FACULTY
OF MATHEMATICS
AND PHYSICS
Charles University

MASTER THESIS

Nicola Burianová

Cross section measurement in reactor spectrum: 55Mn(n,2n), 90Zr(n,2n), 127I(n,2n)

Institute of Particle and Nuclear Physics

Supervisor of the master thesis: Ing. Michal Košťál, Ph.D.
Study programme: Physics
Study branch: Nuclear and particle physics (FJF)

Prague 2018

I declare that I carried out this master thesis independently, and only with the cited sources, literature and other professional sources.

I understand that my work relates to the rights and obligations under the Act No. 121/2000 Sb., the Copyright Act, as amended, in particular the fact that the Charles University has the right to conclude a license agreement on the use of this work as a school work pursuant to Section 60 subsection 1 of the Copyright Act.

In Prague   Nicola Burianová

Title: Cross section measurement in reactor spectrum: 55Mn(n,2n), 90Zr(n,2n), 127I(n,2n)

Author: Nicola Burianová

Institute: Institute of Particle and Nuclear Physics

Supervisor: Ing. Michal Košťál, Ph.D., CVŘ

Abstract: This diploma thesis deals with the validation of spectral average cross-sections (SACS) of ^{55}Mn(n,2n)^{54}Mn, ^{90}Zr(n,2n)^{89}Zr, ^{127}I(n,2n)^{126}I reactions in well-defined LR-0 reactor spectrum. The measurement of SACS for selected reactions is of high interest because they are used for the practical reactor dosimetry. Various experiments for description of neutron field in reactor and detector characterization, which are necessary for validation, are described. The spectral average cross-sections are derived from Net Peak Areas of irradiated samples measured using a semiconductor high purity germanium detector. Obtained result were compared with MCNP6 calculations using ENDF/B-VII.0, ENDF/B-VII.1, JEFF-3.1, JEFF-3.2, JENDL-3.3, JENDL-4, ROSFOND-2010, CENDL-3.1 and IRDFF nuclear data libraries. Notable discrepancies were found in ^{90}Zr(n,2n)^{89}Zr and ^{127}I(n,2n)^{126}I reactions. This thesis also contains a theoretical basis for the interaction of neutrons with matter.

Keywords: spectral average cross-section, validation, (n,2n) reactions, cross-section measurement, 55Mn(n,2n), 90Zr(n,2n), 127I(n,2n), detector characterization, LR-0 reactor

Contents

Introduction

The spectrum-averaged cross sections (SACS) are a crucial quantity for validation of the evaluated reaction cross-sections, presented in the various nuclear data libraries. The measurement of SACS for selected reactions is of high interest because they are used for the practical reactor dosimetry, where these reactions are used to monitor the neutron flux behind reactor vessel and then determine reactor vessel damage. The suitable reaction are included in the International Reactor Dosimetry and Fusion File (IRDFF) [1]. Many of the reactions have already been evaluated, but a substantial portion of them have not yet been validated, or are discrepant, see [2]. These validations can also be used for refining neutron fission spectrum of ^{235}U in region of higher neutron energies. For this is used the ratio of measured spectral average cross-section in reactor spectrum and in spectrum of ^{252}Cf. The fission neutron spectrum of ^{252}Cf, which is taken as standard, is one of the best defined reference neutron spectra.

For cross-sections verification is essential to have a well-defined neutron field in a reactor, due to the MCNP6 calculations of relative flux in the core, and also to have a well-characterized detector where samples are measured. It means to have a good model for calculating efficiency of nonstandard samples, where it is impossible to make detector efficiency by experiment with standard sources. Description of both of these essentials will be described in more detail in the chapters three and four. The first two chapters describe theoretical introduction for neutron and neutron cross-sections. The last two chapters, six and seven, describe the cross-section measurements of ^{90}Zr(n,2n)^{89}Zr, ^{55}Mn(n,2n)^{54}Mn and ^{127}I(n,2n)^{126}I reactions averaged in ^{235}U.

The cross-section are measured at LR-0 reactor because the neutron spectrum in this reactor is similar to prompt fission neutron spectrum of ^{235}U. The LR-0 reactor is a zero power reactor with no fuel burning. Therefore, there are no further contributions to the spectrum from, for example, plutonium.

1. Neutron properties

1.1 Discovery of neutron

The neutron was unknown until the year 1932, when James Chadwick examined experiments where alpha particles from polonium bombarded certain light elements. These experiments was made by Bothe and Becker in 1931 and they examine that some unusually penetrating radiation was produced by alpha particle fell on beryllium. This radiation was not influenced by electric field and that is why they assumed it is gamma radiation. Next experiments made by Irène Joliot-Curie and Frédéric Joliot show that when the radiation from berrilium bombard paraffin, the protons with an energy of about 5.3 MeV are ejected. Scheme of this experiment is in the Figure 1.1. This experimental result were inconsistent with the gamma radiation theory, as can be shown by energy and momentum analysis. Neither Rutherford nor James Chadwick at the Cavendish Laboratory in Cambridge were convinced by the gamma ray interpretation which led Chadwick to perform a series of new experiments. He showed that the new radiation is consisted of uncharged particles with about the same mass as the proton and named these particles as neutrons. For this discovery, Chadwick won the Nobel Prize in Physics in 1935.
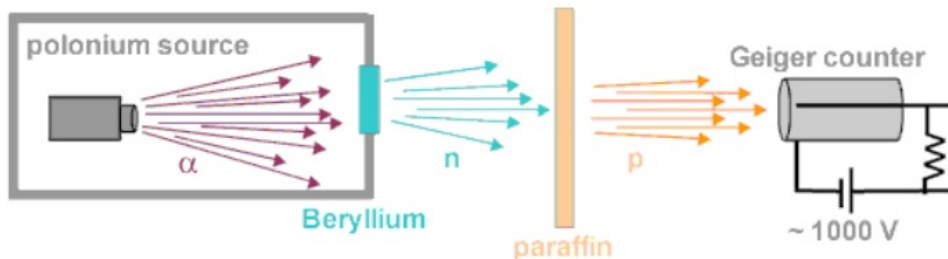

Figure 1.1: The neutron discovery experiment scheme. [3]

1.2 Physical properties of neutron

The mass of a neutron can't be measured by mass spectrometry because the neutron has a neutral electrical charge and is not deflected by a electric field. Neutron mass can be determined for example by measuring momenta of resulting proton and electron from beta decay. Today the known neutron mass is $939.565 \, \mathrm{MeV/c}$, which is slightly heavier than the proton.

A neutron is fermion and thus it has spin 1/2 and obey the Pauli exclusion principle. A neutron spin can by measured by the Stern-Gerlach experiment.

Neutrons have a non-zero magnetic moment, which can be measured by nuclear magnetic resonance, developed by Isidor Rabi in 1938.

A free neutron is unstable and decays via beta decay with a half live 613.9 seconds to a proton, electron and anti-neutrino. This decay involves the weak interaction and is associated with a quark transformation (see the Figure 1.2). Neutrons can travel hundreds of meters in air without any interaction and ionize

only indirectly. Due to the low probability of neutron interaction with matter, neutron radiation is penetrating.
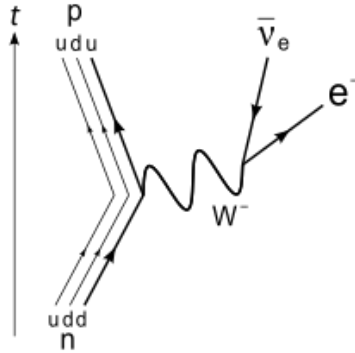
Figure 1.2: The Feynman diagram of neutron beta decay.

All basic neutron properties are summarized in the Table 1.1. Neutrons can also be divided by their kinetic energy into a few groups:

- cold neutrons (0.0 - 0.025 eV)

- thermal neutrons (0.025 eV)

- epithermal neutrons (0.025 - 0.4 eV)

- cadmium neutrons (0.4 - 0.6 eV)

- epicadmium neutrons (0.6 - 1 eV)

- slow neutrons (1 - 10 eV)

- resonance neutrons (1 eV - 300 eV)

- intermediate neutrons (300 eV - 1 MeV)

- fast neutrons (100 keV - 20 MeV)

- ultrafast neutrons (> 20 MeV)

Mass	$939.565 \, \text{MeV/c}^2$
Spin	1/2
Parity	+1
$T_{1/2}$	613.9 s
Electric charge	0 e
μ_n	-1.913 μ_N
Quark content	udd

Table 1.1: Neutron properties.

1.3 Neutron sources and detection

1.3.1 Neutron sources

There are many kinds of neutron sources. Some of them, which are the most significant, will be named.

One of the neutron sources can be the radioisotopes, which undergo a spontaneous fission, which is commonly used the radioactive isotope of ^{252}Cf. It usually emits between 1×10^7 to 1×10^9 neutrons per second, but ^{252}Cf has only 2.6 years half life and that is why the emission significantly decreases over time. At CVŘ is a ^{252}Cf neutron source which emitted approximately 5.5×10^8 neutrons per second in October 2017.

Next neutron sources can be so-called PuBe, AmBe or AmLi. This sources work on the base of mixing a radioisotope that emits alpha particles (such as radium, polonium, or americium) with a low-atomic-weight isotope. Neutrons are produced at a collision of alpha particle with low-atomic-weight isotopes, like beryllium. Mentioned three examples are the most used combinations of alpha particle emitter with the low-atomic-weight isotopes. Typical emission rates for this neutron sources range from 1×10^6 to 1×10^8 neutrons per second.

Another significant neutron source is the nuclear reactor, where the ^{235}U is usually fissioned at two lighter nucleus with a production of 2 - 3 prompt neutrons. Another neutrons are produced by following beta decay of fission fragments.

The particle accelerator can also be used as neutron source. Here, neutrons are produced by bombarding the target material with accelerated protons.

Neutrons are also in our natural background. This background is caused by muons from cosmic ray interaction with the atmosphere.

1.3.2 Neutron detection

As it was already mentioned, neutrons have neutral electrical charge and cannot ionize matter directly. Neutron energy is thus converted to energy of some charged particle before it's detection. It can be converted by elastic scattering and neutron capture. Generally, every type of neutron detector must be equipped with a converter and one of the conventional radiation detectors (scintillation detector, gaseous detector, semiconductor detector). Neutron detectors can be divided into two types: active detectors and passive detectors.

One of the options to detect neutrons is adapted gas proportional detector. Neutrons don't cause ionization, but with the addition of a nuclide with high neutron cross-section is possible to detect gamma radiation from neutron interaction. The commonly used nuclides for this purpose are ^{3}He, ^{6}Li, ^{10}B and ^{235}U. These detectors are active.

Other options are scintillation detectors, which are also active and measure the fast neutrons. At CVŘ are used organic stilbene neutron detectors ($C_{14}H_{12}$). Stilbene crystals are especially good at detecting fast neutrons, which are given off by nuclear materials, like plutonium. The neutron flux and spectrum measurement are based on proton recoil detection in the stilbene crystal. The example of stilbene crystal is in the Figure 1.3.

The last to be mentioned are neutron activation detectors, which belong to passive types of detectors. Here, neutrons are detected from activity measurement

Figure 1.3: Stilbene crystals. [4]

of produced nuclei. The chosen target is irradiated by neutrons and subsequently the activity of produced nuclei is measured by HPGe detector. For monitoring, it should be used materials with well known cross-section, e.g. low uncertainty in cross section. This is met for example in Au ((n,γ) reaction is sensitive to thermal neutrons, (n,2n) reactions is suitable monitor of fast neutrons with energies > 10 MeV)), Ni ((n,p) reaction sensitive for fast neutrons) Al (n,α) reaction also sensitive to fast neutrons. These detectors are not spectrometric, they measure only integral over neutron spectrum. Examples of activation foils are in Figure 1.4.
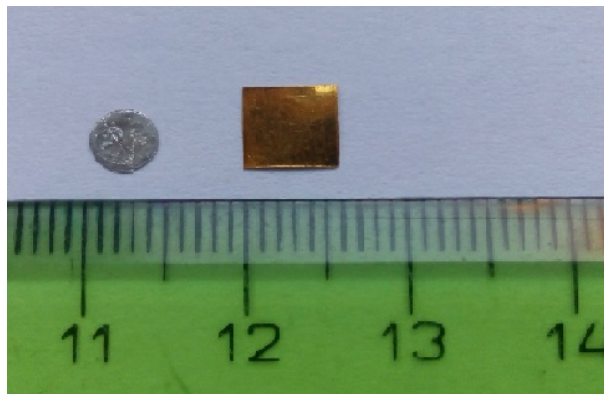

Figure 1.4: Example of activation foils - 1%Au left, 100%Au right.

2. Neutron interaction with matter

Neutron is neutral particle, therefore it is deviating from a straight path only when it collides with a nucleus and is scattered or absorbed. The mean distance that neutron travels between collision with a nucleus is a mean free path length λ which can be calculate from

$$\lambda = \frac{1}{\Sigma},\qquad(2.1)$$

where Σ is macroscopic cross-section which is derived from microscopic cross-section σ by

$$\Sigma = N\sigma,\qquad(2.2)$$
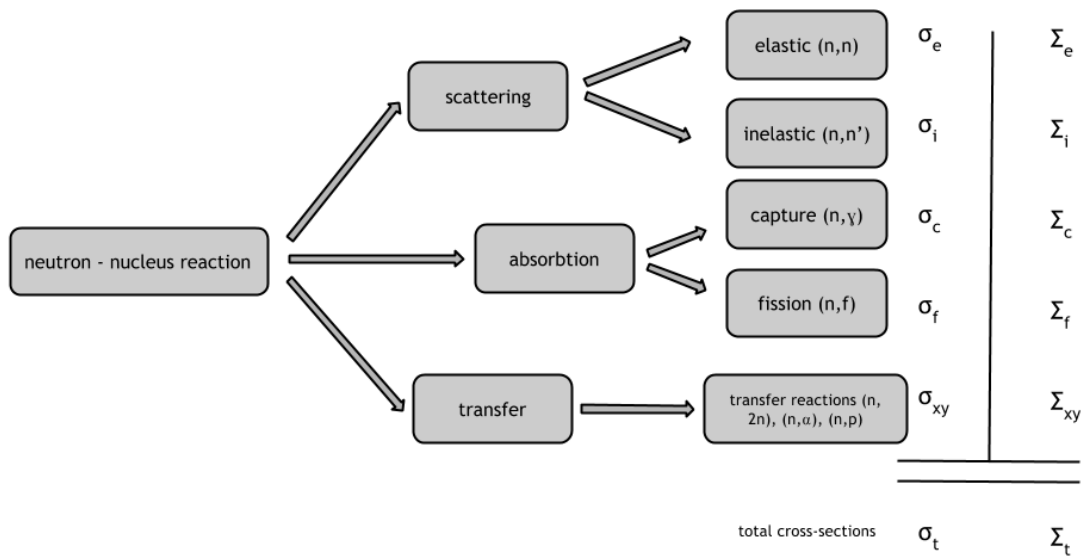
where N is nuclei density.

Figure 2.1: Neutron interactions. [5]

In the picture 2.1 we can see scheme of possible neutron interactions with the matter and each part will be described in more detail.

2.1 The types of neutron interaction

2.1.1 Neutron scattering

The scattering can be elastic (n,n) or inelastic (n,n'). During elastic interaction, no neutron energy is transferred into nuclear excitation and only the neutron direction is changed. During the inelastic scattering, some energy of the incident neutron is absorbed to the recoiling nucleus and the nucleus remains in the excited state. The neutron is than emitted with a lower kinetic energy. The momentum

is conserved in an inelastic collision, but the kinetic energy of the system is not conserved. The cross-section of the neutron scattering (σ_s) is given as a sum of elastic σ_e cross-section and inelastic σ_i cross-section.

2.1.2 Neutron absorption

The neutron absorption reaction is the most important type of reactions that take place in a nuclear reactor. The absorption reactions are reactions, where the neutron is completely absorbed and compound nucleus is formed. The most important absorption reactions are divided by the exit channel into two reactions - neutron capture and nuclear fission.

For non-fissionable nuclei is only the first reaction (neutron capture) possible. It is a reaction, in which the incident neutron is completely absorbed and compound nucleus is formed. The compound nucleus then decays to its ground state by gamma emission. This process can occur at all incident neutron energies, but the probability of the interaction strongly depends on the incident neutron energy and also on the target energy (temperature). The cross-section of this reaction (n,γ) is denoted by σ_c.

During the second reaction (nuclear fission) the nucleus of target is split into two ore more lighter nuclei. The fission process often produces free neutrons, photons and releases a large amount of energy. But not all neutrons are released at the same time following fission. From this point of view we usually divide the fission neutrons into two groups - prompt neutrons, which are emitted directly from fission and they are emitted within very short time of about 10^{-14} second, and delayed neutrons which are emitted by neutron rich fission fragments. These precursors usually undergo beta decay but a small fraction of them are excited enough to undergo neutron emission. The fact the neutron is produced via this type of decay and this happens orders of magnitude later compared to the emission of the prompt neutrons, plays an extremely important role in the control of the reactor.

The cross-section of (n,f) reaction is denoted by σ_f. The fissionable materials can undergo both of absorption reactions and its cross section is thus $\sigma_a = \sigma_c + \sigma_f$.

2.1.3 Transfer reactions

The transfer reaction can be also divided into two sections - neutron emission as are (n,2n),(n,3n)...(n,xn) and charged particle ejection as for example are (n,α) and (n,p).

If the kinetic energy of an incident neutron is sufficient the double, triple, or more, neutron emission may take place. The probability of such reactions increases with increasing incident neutron energies.

Charged particle reactions are usually associated with formation of a compound nucleus, which is excited to a high energy level, that such compound nucleus can eject a new charged particle while the incident neutron remains in the nucleus. After the new particle is ejected, the remaining nucleus is completely changed, but may or may not exist in an excited state depending upon the mass-energy balance of the reaction.

2.2 Neutron cross-section

The cross-section is an effective area that quantifies the likelihood of certain inter-action between an incident object and a target. In nuclear physics, it characterizes the probability that a nuclear reaction will occur. It is denoted by σ and the unit is barn (b), which is equal to $10^{-28}\,\mathrm{m}^2$. The total (neutron) cross-section is given as the sum of all upper mentioned cross-sections:

$$\sigma_t = \sigma_s + \sigma_a + \sigma_{xy}. \tag{2.3}$$

2.2.1 Regions of neutron capture cross-section

The neutron capture cross-section can be divided into three regions according to incident neutron energy (see the Figure 2.2).

- thermal region $(0.025\,\mathrm{eV}$ - $1\,\mathrm{eV})$

- resonance region $(1\,\mathrm{eV}$ - $1\,\mathrm{keV})$

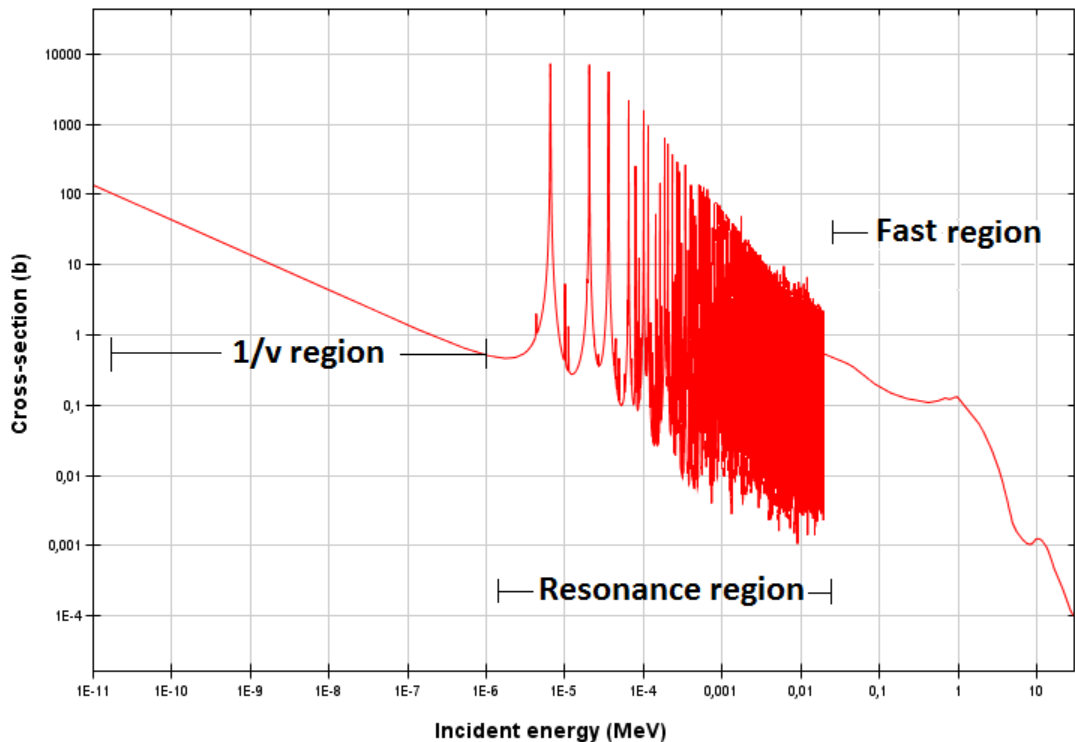- fast region $(1\,\mathrm{keV}$ - $10\,\mathrm{MeV})$

Figure 2.2: Neutron capture cross-section with regions at ^{238}U. [5]

As can bee seen from the Figure 2.2, the largest cross sections are in the res-onance region. This region corresponds to the energies of an compound nucleus. The formation of resonances is caused by the quantum nature of nuclear forces. Each nuclear reaction is a transition between different quantum discrete energy levels. If the sum of energy of the neutron and the energy of target nucleus is

equal to a compound nucleus at one of the excitation states, a resonance can be created. So the first resonance corresponds to the first excitation energy of a compound nucleus. At high excitation energy, the gap between two compound states is very small and the widths of resonances may reach the order of the distances between resonances. Therefore, at high energies no resonances can be observed.

The theory of compound nucleus was formed to explain the resonances in neutron capture cross-sections. The compound nucleus is an intermediate state of reactions. It is one of the excited states of the nucleus formed by the combination of the incident neutron and target nucleus. If the target ^{238}U is bombarded with neutrons, the compound nucleus ^{239}U is created. This compound nucleus is excited, or in a high-energy state, and unstable.

The formation of compound nucleus takes a period of time approximately equal to the time interval for the bombarding particle to travel across the diameter of the target nucleus (about 10^{-21} second). Secondly, after a relatively long period of time (typically from 10^{-19} to 10^{-15} second) and independent of the properties of the reactants, the compound nucleus decays, usually into an ejected small particle (neutron, alpha, proton) and a product nucleus.

3. Characterization of used neutron field in LR-0 reactor

For measuring and validation of spectral average cross-sections is necessary to have a well-defined neutron field in a reactor, where the samples are irradiated. Several experiments ([6], [7], [8], [9], [10]) were performed to compare measured results with the computational prediction using mathematical model of a reactor core. In order to verify the model, mainly two factors are needed - critical experiment must correspond to model results of critical height and also power profile. For greater computational model verification certainty two other experiment were performed - stilbene measuring of neutron spectra and spatial distribution of selected reaction rates.

As it was mentioned in the introduction, the LR-0 reactor was chosen for measuring and validation because of its better-described neutron spectrum. This spectrum is near the prompt fission neutron spectrum of ^{235}U, as can be seen in the figure 3.9. Fuel burning occurs in the second reactor in CVŘ, LVR-15, and thus to its transforming into plutonium and other elements. In this reactor spectrum is then not only uranium spectrum, but also the spectrum of plutonium and the nontrivial correction is necessary to perform.

3.1 LR-0 experimental reactor

The LR-0 is a zero power light water pool type reactor. The reactor is used for experimental measurement of core characteristic for VVER reactors, which are in nuclear power plants in Czech Republic. Continuous nominal power is $1\,\mathrm{kW}$ with a thermal neutron flux of about $10^9\,\mathrm{cm^{-2}s^{-1}}$ and a fast (above $1\,\mathrm{MeV}$) neutron flux of $2\times10^8\,\mathrm{cm^{-2}s}$ $^{-1}$. The LR-0 reactor has been designed in a universal manner, suitable for physics experiments on VVER-type active zones with a wide range of cartridge quantities, fuel enrichment, along with various concentrations of H_3BO_3 in the moderator and configurations of absorptive elements in the cartridges. A very important part of research is the experimental verification of radiation damage to materials used in internal reactor assemblies and VVER reactor vessels [11]. The scheme of LR-0 reactor is in the Figure 3.1.

3.2 Critical parameter

The measurements were performed in LR-0 reactor with the fuel configuration as is in the Figure 7.2, but with an empty dry channel in the middle. During this experiment, the critical height H_{cr} of reactor were detected by measuring the number of neutrons in the reactor core. The measured H_{cr} were after compared with calculated H_{cr}.

Criticality is obtained by adjusting the moderator level. When the moderator level is slightly above H_{cr}, reactivity ρ may be expressed via a one-group
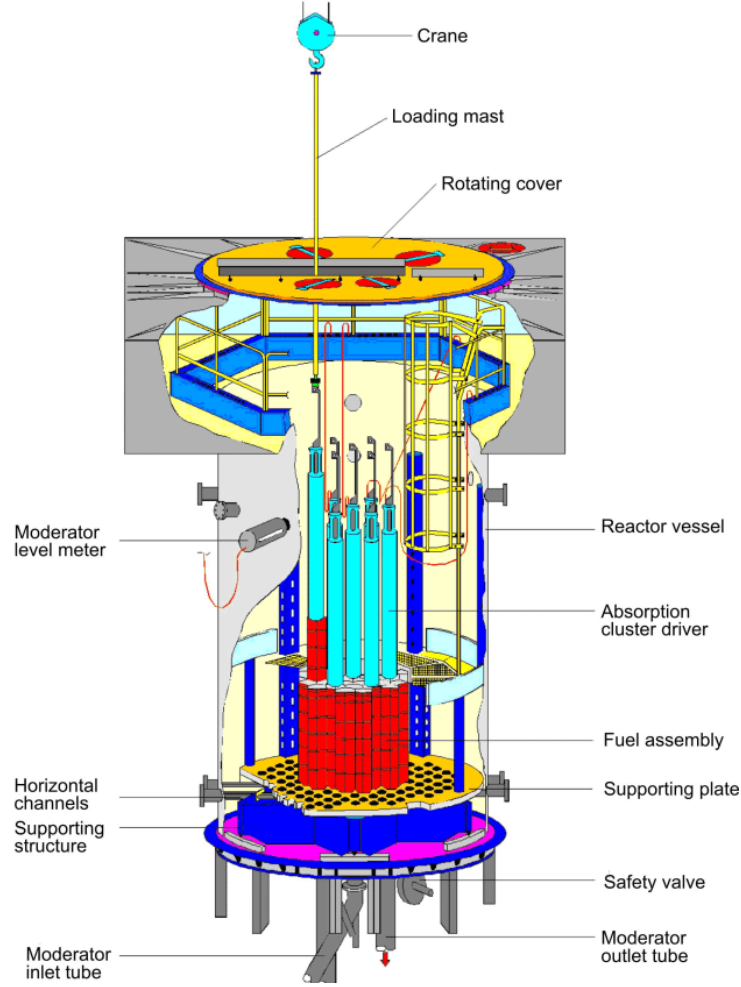
Figure 3.1: LR-0 scheme. [11]

asymptotic approximation

$$\rho(H) = \frac{C}{(H_{cr} + \lambda_z)^2} \left[\frac{1}{1 + \frac{H - H_{cr}}{H_{cr} + \lambda_z}} - 1 \right]; \rho = \frac{k_{eff} - 1}{k_{eff}}, \qquad (3.1)$$

where constant $C = \frac{M^2 \pi^2}{k_\infty}$, M^2 is migration area and λ_z is the axial extrapolation length.

If reactivity is less than 25 cents, a Taylor expansion of relation 3.2 around H_{cr} may be used. Reactivity for various moderator heights above the critical level was measured using the inverse kinetics method with time-dependent neutron counts. The digital reactimeter and data acquisition were implemented using an independent EWS computer system:

$$\rho(H) = f(H, a_1, a_2) = a_1(H - a_2)\left(1 - \frac{3}{2}\frac{H - a_2}{a_2 + \lambda_z}\right), \qquad (3.2)$$

where $a_1 = \frac{\delta \rho}{\delta H}$ and $a_2 = H_{cr}$.

The critical moderator level reactivity coefficient and associated standard deviation are determined by non-linear regression analysis of relation 3.2 or from its linear approximation.

The tolerance of the measured H_{cr} for the LR-0 reactor, based on level meter manufacturer technical data is $0.003\,cm$. The total uncertainty of H_{cr} at the 1σ level is determined from the tolerance of the level meter and its calibration. The uncertainty of the level meter calibration is determined by the precision at witch the electrical needle is positioned. This is an electric contact used for repeated level meter tests, which is fixed on the vessel wall at a hight of $10\,cm$ with uncertainty of $0.05\,cm$. The combined uncertainty of the critical water value H_{cr} is $0.058\,cm$.

These experiments were also performed with graphite inside the dry central channel. The various configurations of the graphite insertion are shown in the Figuge 3.2. The comparison of experiment result with calculations using various libraries is plotted in the Figure 3.3.
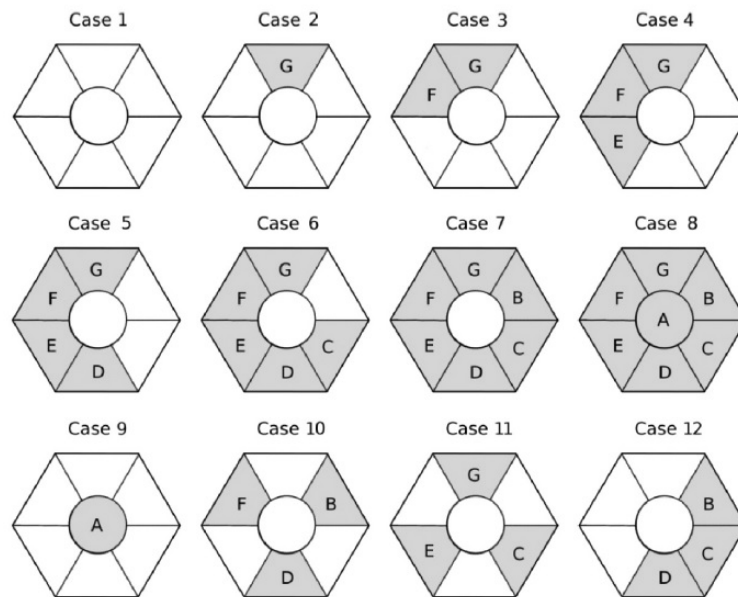

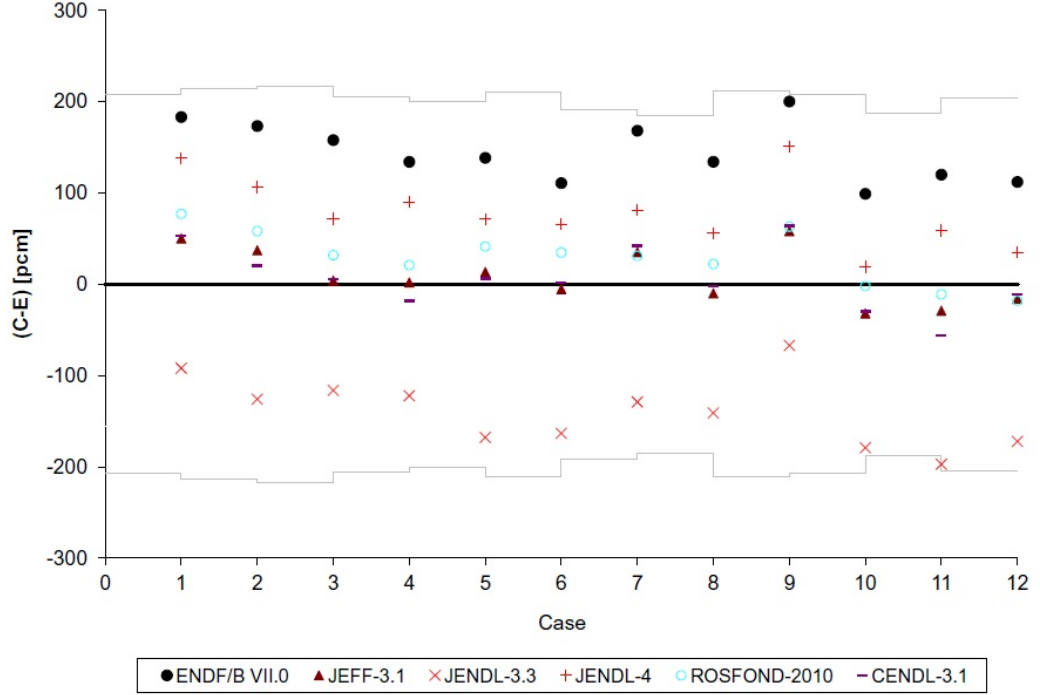Figure 3.2: Various configurations of the graphite insertion. [9]

Figure 3.3: Comparison of experimental results with calculations using various libraries. Experimental uncertainty is depicted by the gray envelope. [9]

3.3 Power profile of LR-0 reactor

The power profile of the LR-0 reactor were measured by gamma activity of single pins from fuel. This can be done because the fuel is decomposable. The activity of chosen pins (outer diameter 0.915 cm, active length 125 cm), see the Figure 3.4, were measured by High Purity Germanium (HPGe) detector placed in the lead shielding, see the Figure 3.5. The measurement were carried out for 15 intervals from 10.4 cm to 85.4 cm, each of length 5 cm. Lead shielding was used to reduce the contribution from non-collimated parts of fuel pin, but the results had to be corrected for shielding transmissivity. More information about this correction can be found in [12].

The fuel pin rotated during the measurement to compensate for non-uniform fission product distribution.The device, where the pins were held, provides sequential axial movements with arbitrary distance between points of gamma measurement. The photo of this device in laboratory is in the Figure 3.6.

After irradiation, the Net Peak Area (NPA) of the 1383.9 keV peak from ^{92}Sr decay, were measured. This photon decay was chosen due to its suitable gamma energy and half-live. There is also no need to apply the coincidence correction. The ^{92}Sr fission product was induced during 2.5 h of irradiation at a monitored power . The pulse rate in a selected gamma energy peak were corrected for the radioactive decay from the initial value at reactor shutdown time. The residual gamma activity of all measured pins were determined before irradiation. The used pins had negligible background activity in the studied regions.
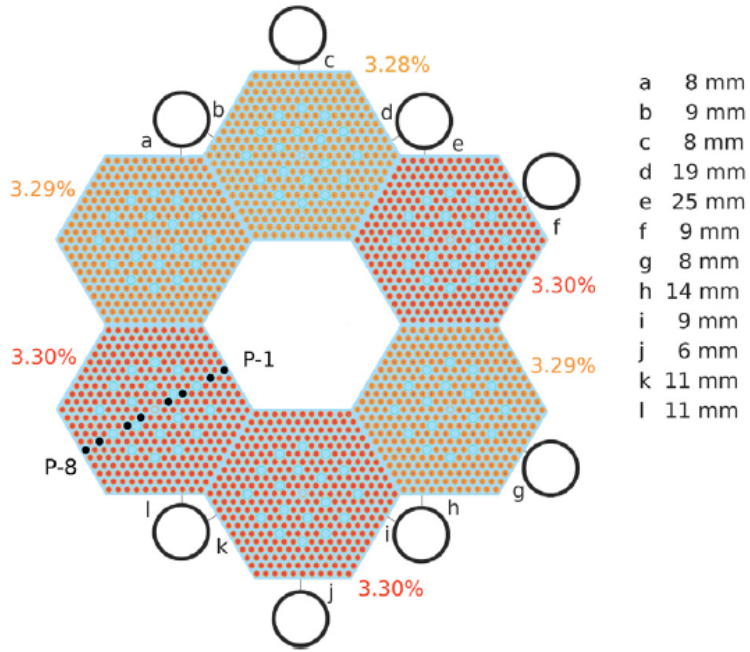
Figure 3.4: Radial cross-section of the core with specified enrichment and measured pins (P-1...P-8). The distances of power monitor channels, labeled a to l, are measured perpendicular to the nearest row of pins. [7]
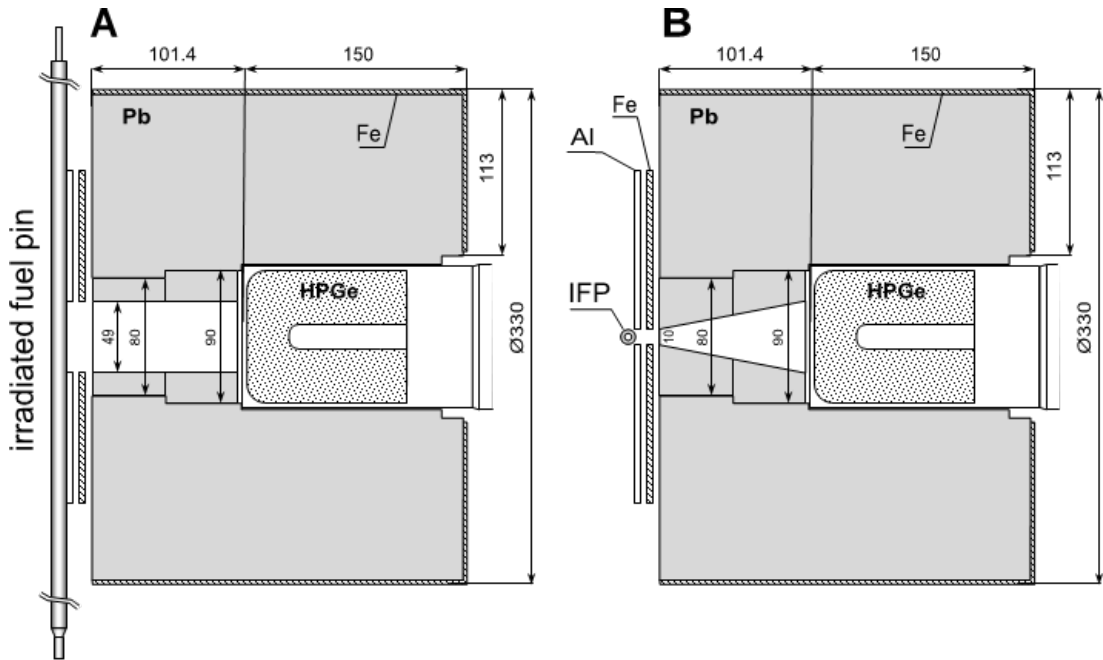

Figure 3.5: Geometry of HPGe detector (Left side (A) is vertical direction, right side (B) is horizontal). [7]

The uncertainties of counts rates were about $0.8 - 3\%$ and included the gross peak area, the Compton continuum area, the background, energy and peak shape calibration parameters, the reactor shutdown time and radionuclide decay during the measurement uncertainties.

Figure 3.6: The laboratory with gamma spectrometry systems for fuel pins measurement. [7]

The axial power profile was evaluated by the equation

$$F_j^i = NPA_j^i(0) \cdot \frac{Tf_j^i}{\eta_j^i \cdot \epsilon \cdot \lambda \cdot N_j^i(0)}, \tag{3.3}$$

where $N_j^i(0) = \sum_{m=1}^{N} q_i^j \cdot (1 - \exp[-\lambda \cdot (\tau_n - \tau_m)]) \cdot \exp[-\lambda \cdot (T_{irr} - \tau_n)]$, F_j^i is the fission rate of the i-th pin and j-th position on the measured fissile column, $q_i^j(t)$ is the spectral weighted fission yield at the j-th position of i-th pin, T_{irr} is the time of irradiation, τ_m is the boundary of the time interval during irradiation, $NPA_j^i(0)$ is the measured NPA of ^{92}Sr nuclei at a defined position of the i-th pin, Tf_j^i is the calculated correction of gamma transmission from the fuel pin region adjacent to the measured one, λ is the decay constant, η_j^i is is the calculated HPGe efficiency in the 1383.9 keV peak of the i-th pin and j-th position, ϵ is the gamma branching ratio in the 1383.9 keV peak and N is the number of time steps with stable moderator level.

The comparison of measured results with calculations from ENDF/B-VII data library (C/E) is in the Table 3.1 and also in the Figure 3.7. It can be seen, that the experiment and calculations are with a good agreement under the water level, which was 55.4 cm. Due to the fact, that all samples used for cross-section validation are irradiated in the position under the water level, this MCNP computation model of LR-0 reactor is sufficient. More information about this experiment can be found in [7].

| Axial position [cm]	P-1 [%]	P-2 [%]	P-3 [%]	P-4 [%]	P-5 [%]	P-6 [%]	P-7 [%]	P-8 [%]
10.4	5.8	4.2	6.9	4.1	2.9	2.0	3.2	-0.7
15.4	2.4	2.2	1.9	3.4	-0.1	-0.8	1.0	1.0
20.4	4.0	2.7	0.8	1.4	3.4	1.1	0.5	5.2
25.4	3.0	0.9	3.9	1.7	3.3	4.7	3.5	6.2
30.4	-0.8	1.4	1.2	0.7	1.6	0.0	0.7	-0.5
35.4	-1.8	0.2	-0.9	0.9	-1.6	0.9	-0.4	1.2
40.4	-4.3	-3.8	-2.8	-3.7	0.0	0.2	-1.3	-4.8
45.4	2.8	2.8	2.8	2.8	3.0	3.0	3.1	3.1
50.4	3.0	3.1	3.2	3.3	3.6	3.6	3.8	3.9
55.4	3.4	4.1	5.1	5.4	5.5	5.9	5.5	6.4
60.4	2.8	3.1	3.6	3.9	5.0	4.8	4.2	4.2
65.4	2.9	3.1	3.3	3.4	4.8	4.5	4.2	4.2
70.4	2.9	3.1	3.3	3.4	3.8	3.7	3.5	3.5
75.4	2.9	3.2	3.5	3.6	4.1	4.0	3.7	3.8
80.4	3.0	3.3	3.7	3.9	4.3	4.2	4.0	4.0

Table 3.1: C/E-1 comparison of axial power profile.
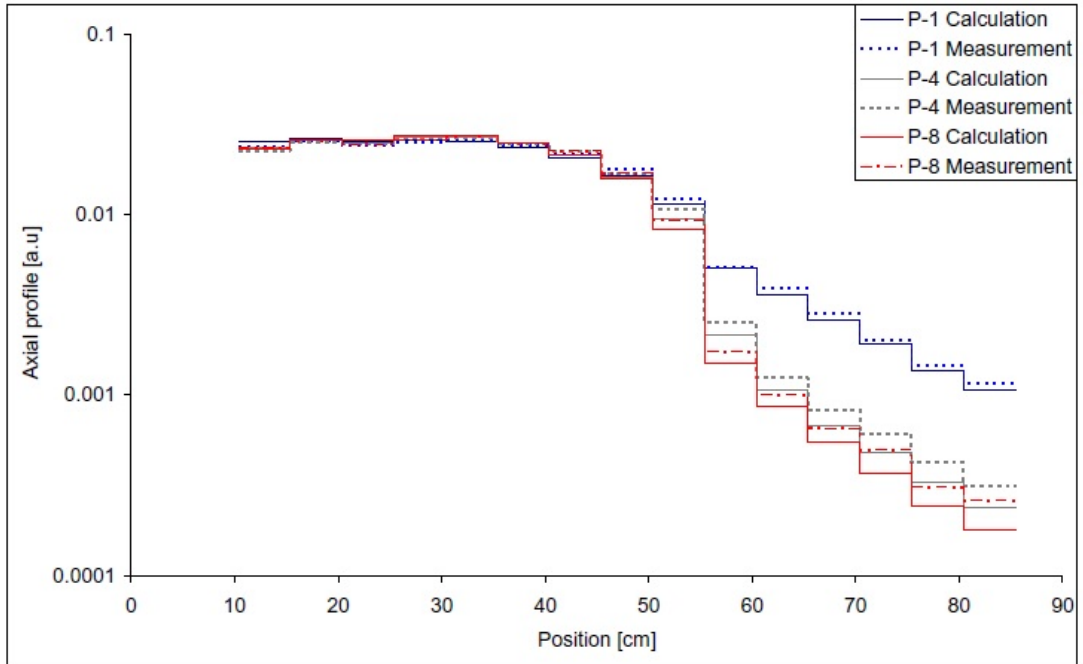
Figure 3.7: Comparison of calculated and experimental axial profiles. [7]

3.4 Measurement of fast neutron spectra by stilbene detector

For a greater certainty of mathematical model of the core and irradiation cavity the neutron spectrum was also measured by scintillation stilbene detector via the proton-recoil method. The detector was placed in the dry experimental channel. The comparison of calculation and measurement can be seen in the Figure 3.8.

Reactions under study cross-sections have a thresholds above 10 MeV of neutron energy, therefore the measurement could only be done in the area of fast neutrons. More informations about this experiment can be found in [8].
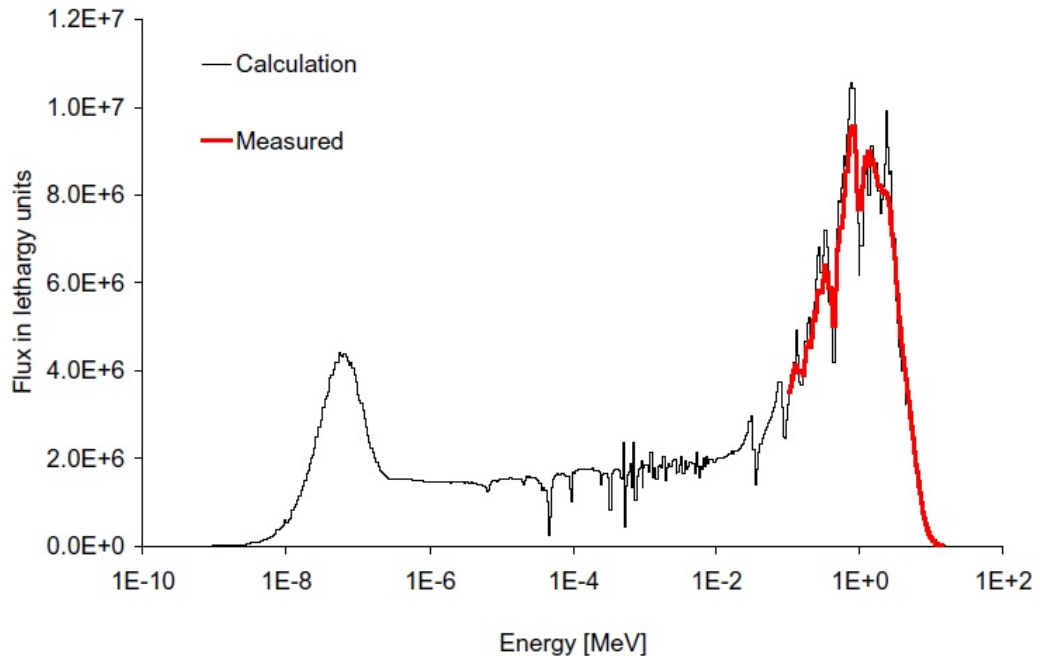

Figure 3.8: Comparison of calculated and measured neutron flux - stilbene detector was placed in the same reactor dry channel in center of core as were placed irradiated samples. [8]

The measured neutron spectrum in LR-0 reactor were also compared with the ^{235}U prompt fission neutron spectra (PFNS) from ENDF/B-VII.0 [14], ENDF/B-VII.1 [15] and CIELO [16] nuclear data libraries. In the Figure 3.9 can be seen that calculated ^{235}U PFNS is indistinguishable from LR-0 spectra in region above 5.5 - 6 MeV. In fast energy region, most significant variations between ^{235}U PFNS in CIELO and ENDF/B-VII.1 library, are in region above 10 MeV. The measurement of spectral average cross-sections in this area of energies shows that the more correct nuclear data library for PFNS of ^{235}U in higher energies is CIELO, where are less discrepancies in comparison with the ENDF/B-VII.1 library. This can be seen in the Table 6.5. These cross-section verifications are therefore important also for refining PFNS of ^{235}U in region of higher neutron energies (above 10 MeV).

3.5 Spatial distribution of neutron flux

During this experiment an aluminum holder with activation foils were placed into the dry channel. The scheme can be seen in the Figure 3.10. The critical height of the moderator during irradiation was 55.48 cm and irradiation was carried out approximately 10 hours at power 5 W. The mainly used activation foils were Au and Ni. In the aluminum holder were also activation foils of Mn, Y, Ta and ^{54}Fe for cross-section validation. The details of calculated flux profiles in the
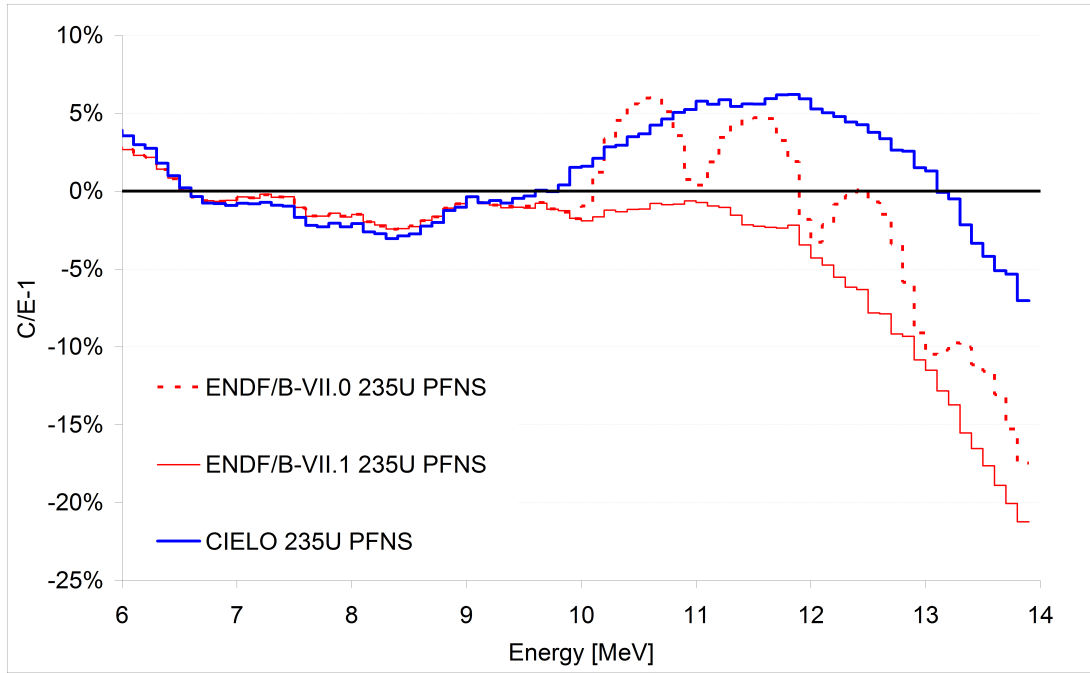
Figure 3.9: Identity between LR-0 and ^{235}U PFNS in ENDF/B-VII.0, ENDF/B-VII.1 and CIELO nuclear data libraries. [10]

irradiation cavity in the core is plotted in the Figure 3.11 (radial profile) and in the Figure 3.12 (axial profile). It can be seen that in the part, where samples are irradiated, the non-homogeneities are negligible. More informations about this experiment can be found in [6].
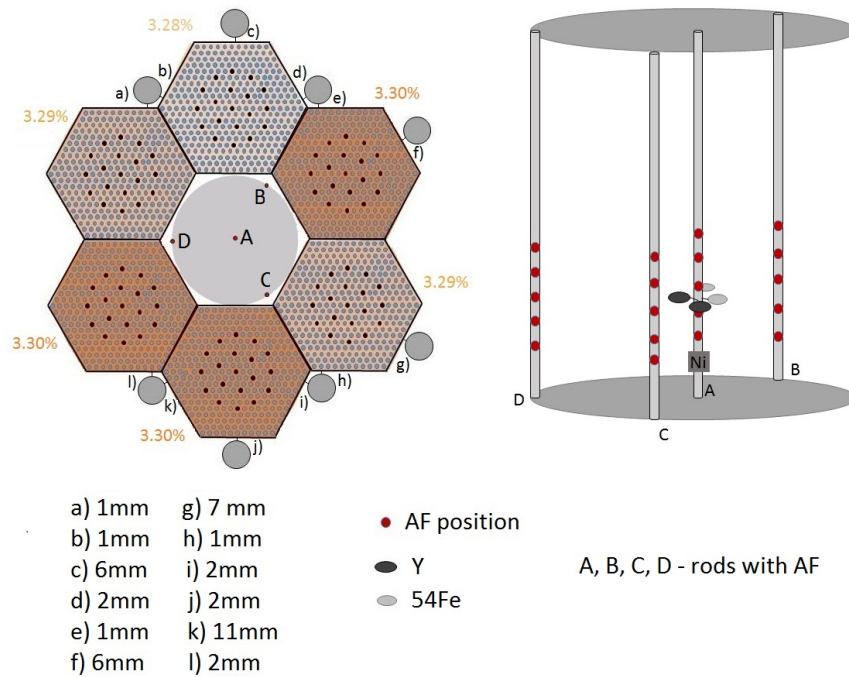

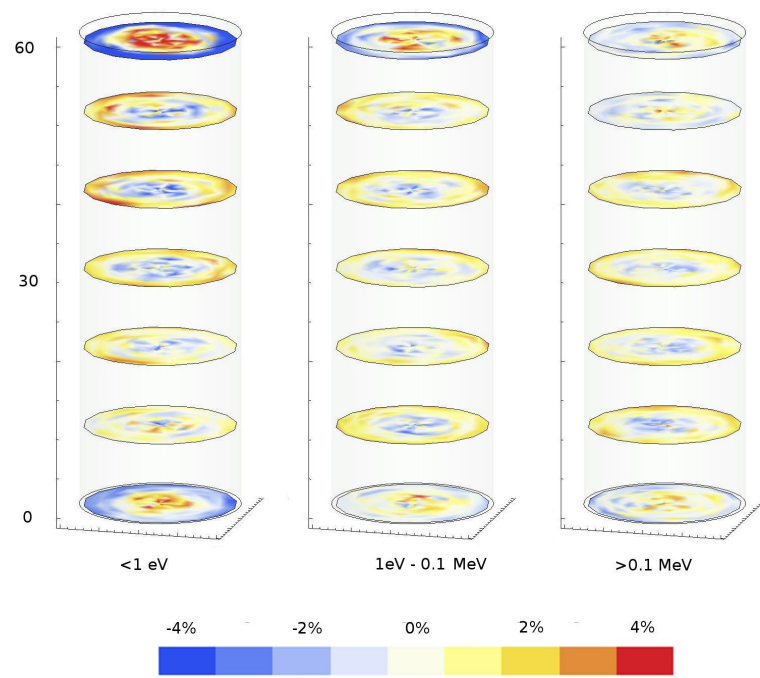Figure 3.10: Axial view of reactor core and special activation foils holder.

Figure 3.11: Calculated non-homogeneities in radial sense. [6]
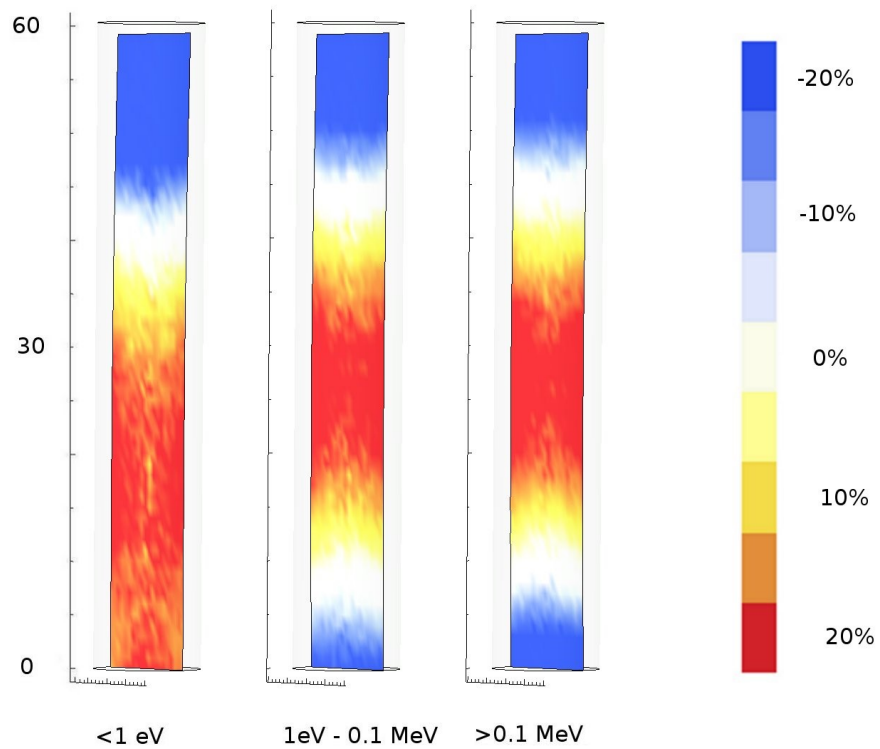
Figure 3.12: Calculated non-homogeneities in axial sense. [6]

21

4. Characterization of semiconductor HPGe detector

4.1 Radiograms

A HPGe semiconductor detector was irradiated in pure ^{137}Cs gamma source at a distance of 5 m at ČMI in Czech Republic. The film was placed 1.5 mm behind the detector and was irradiated 2 hours. From the resulting radiogram were subsequently measured detector parameters. Due to the divergence of the ^{137}Cs source beam, it was necessary to make a correction. This correction was obtained from the ratio of measured detector diameter from radiogram and real detector diameter measurement. Divergence factor was 1.016. The picture of radiogram is in the Figure 4.1 and the measured values of the detector are listed in the Table 4.1. It was found that the data provided by the manufacturer differed from the radiogram data.

	Measured value [cm]	Uncertainty [cm]
Crystal radius	3.003	0.010
Crystal length	5.525	0.020
Hole radius	0.482	0.011
Hole length	4.420	0.035
Cap thickness (aluminum)	0.143	0.013
Pin radius	0.331	0.024
Pin contact length	0.369	0.026
Gap thickness (vacuum)	0.480	0.018

Table 4.1: Experimentally determined detector parameters from radiogram.

4.2 Insensitive layer

For the detector model it was also necessary to measure the thickness of detector insensitive layer. A source collimator, that could be positioned in two different ways, was designed. The photon beam from ^{241}Am could hit the detector surface at two different angles of incidence relative to the crystal surface - 45 ° and 90 °. The source of ^{241}Am was chosen because of its low full energy peak, 59.54 keV. This energy is low enough that the difference between the penetration across the insensitive layer at two angles is recognizable in measured NPA. The photo and scheme of source collimator is in the Figure 4.2.

The measurements were performed at 33 points on the front of the detector surface and at 12 points on the side of the detector, see the Figure 4.3. Each point was measured twice, at 90 ° and 45 ° of the incident radiation. Since there is a gap between the end cap surface and the crystal surface, the collimator must be moved sideways between the 90 ° and 45 ° measurements, so that the photon beams hit the same point on the crystal surface during both measurements. For

Figure 4.1: Picture of detector radiogram.

determination of this shift was needed to determine gap thickness and aluminum (cap) thickness. These distances were taken from radiogram, see the Table 4.1.

The thickness of the insensitive layer d_{Ge} was calculated from the relative change in the count rate between the two angles by the equation [17]

$$d_{Ge} = ln\left(\frac{\dfrac{N_{45}}{N_{90}}}{e^{-\mu_{Al}d_{Al}(\sqrt{2}-1)} \times e^{-\mu_{mylar}d_{mylar}(\sqrt{2}-1)}}\right)\Bigg/ -\mu_{Ge}(\sqrt{2}-1), \qquad (4.1)$$

where N_{45} is the count rate (NPA/t_{live}) at 45°, N_{90} is the count rate at 90°, μ_{Al}, μ_{Ge}, μ_{mylar} are the linear attenuation coefficients, d_{Al} is is the total thickness of aluminum and d_{mylar} is the total thickness of Mylar.

The insensitive layer thickness results are listed in Table 4.2 and displayed in Figure 4.4. The average value of insensitive layer thickness, which was used in MCNP detector model, is $0.158 \pm 0.003\,\text{cm}$ on the front and $0.121 \pm 0.003\,\text{cm}$ on the side.
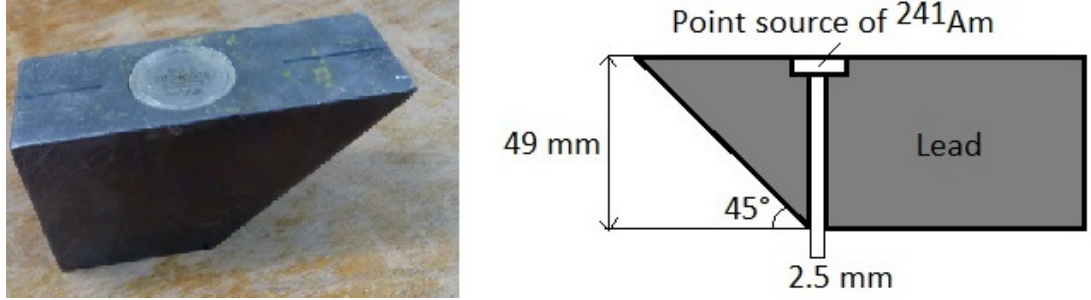
Figure 4.2: The photo (left) and the scheme (right) of the lead collimator for the insensitive layer thickness measurement.

position	d_{Ge} [mm]	position	d_{Ge} [mm]	position	d_{Ge} [mm]
detector center	1.49	A	1.58	K	1.42
1	1.35	X	1.51	L	1.60
2	1.37	D	1.33	Y	1.18
3	1.65	E	1.54	P	1.35
V	1.51	F	1.62	Q	1.44
-1	1.37	T	1.59	R	1.54
-2	1.45	O	1.39	S	1.64
-3	1.52	N	1.45	I	1.31
Z	2.04	M	1.70	H	1.37
C	1.40	W	1.52	G	1.72
B	1.56	J	1.29	U	1.29
1a	1.47	2b	1.03	3c	1.40
1b	1.00	2c	1.26	4a	1.83
1c	1.22	3a	1.03	4b	1.17
2a	1.14	3b	1.38	4c	1.26

Table 4.2: Measured insensitive layer thickness.
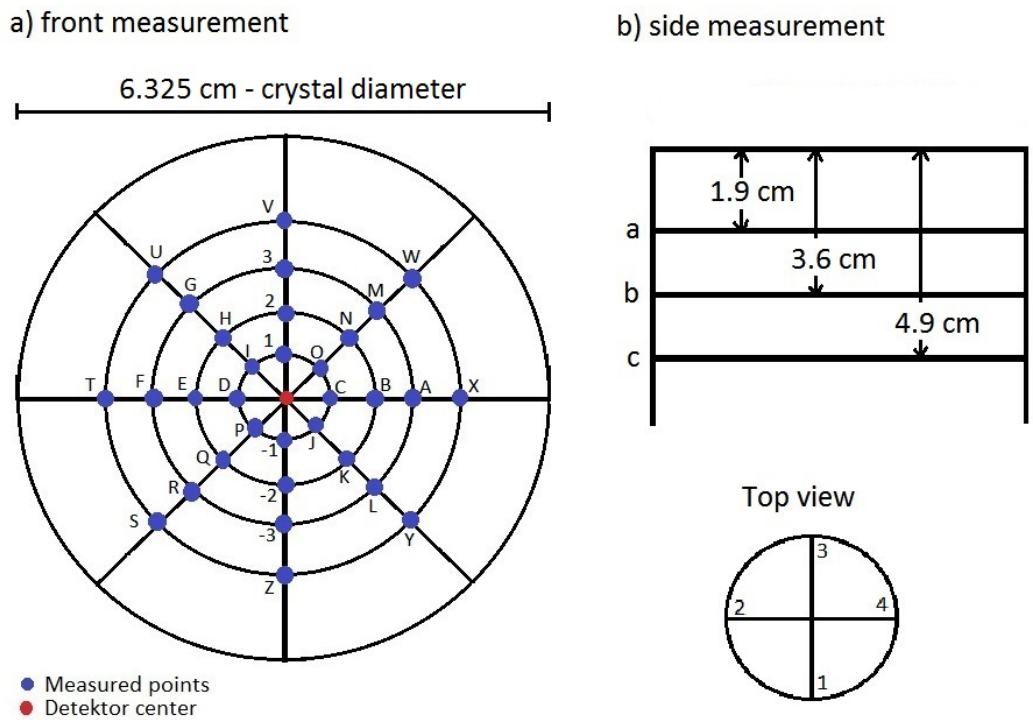
Figure 4.3: Insensitive layer measurement scheme - all distances between measured points on black lines are 6 mm.
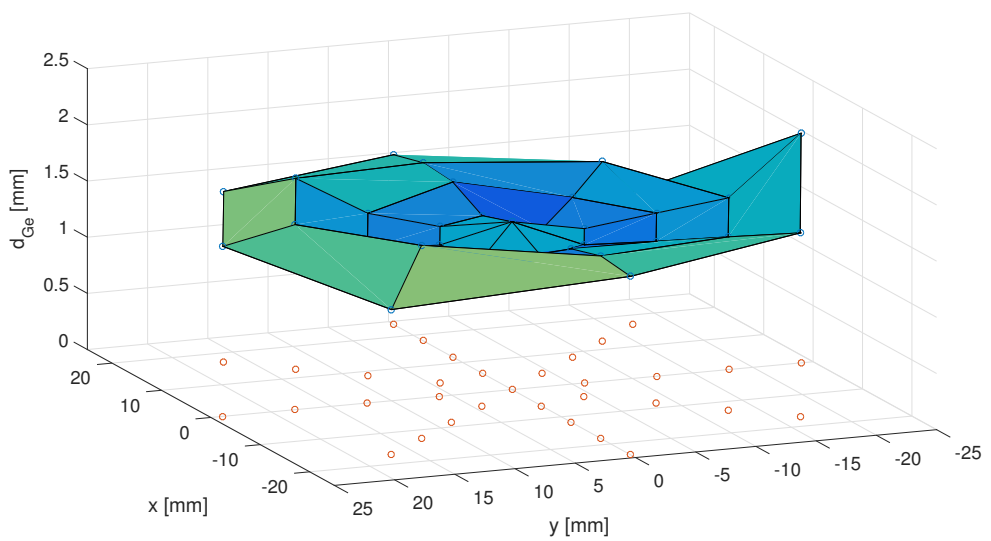
Figure 4.4: Graph of insensitive layer thickness results on the front of the detector.

5. Manufacture of artificially radioactive materials

Artificial radionuclides are prepared using practically all types of nuclear reactions. For production, any source of particles causing the reaction can be used. Thus, it can be accelerator or reactor. The reaction rate q (the rate of radionuclide formation) is directly proportional to the particle flow density I, which the target is irradiated, to the reaction cross section σ and to the number of target nuclei N_t, so than $q = N_t \sigma I$. If the product is not radioactive, the number of produced nuclei increase linearly with the time ($N(t) = qt$), see the Figure 5.1 the curve 1. But if the product is radioactive then the number of produced nuclei is dependent on the irradiation time t_{irr} by the equation

$$N(t) = \frac{q}{\lambda}(1 - e^{-\lambda t_{irr}}), \qquad (5.1)$$

which is the curve 2 in the Figure 5.1.
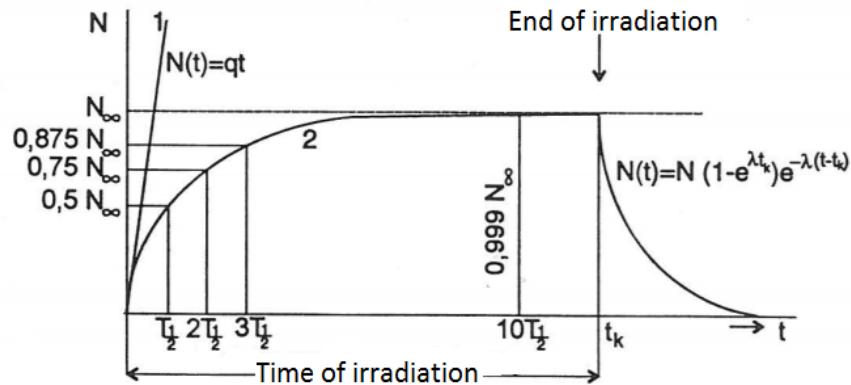
Figure 5.1: Time of irradiation dependence on half live of resulting radioisotope.

The maximum number of radionuclide nuclei, that can be obtained during the time period $t_{irr} \to \infty$, is $N(\infty) = \frac{q}{\lambda}$. When the $t_{irr} = T_{1/2}$, then $N(T_{1/2}) = \frac{1}{2}N(\infty)$.

The irradiation time is dependent on the half live of the resulting radioisotope. As can be seen from Figure 5.1, the maximum (saturation) amount of radioactive material is produced already during ten half lives. In practice the irradiation time is shorter than ten half lives. For a short-lived radioactive materials is the maximum reached very early. For long-term radioisotopes is impossible to irradiate them to reach the saturation activity A_{sat}. The activity of irradiated sample is

$$A = \lambda N(t) = q(1 - e^{-\lambda t}). \qquad (5.2)$$

The saturation activity ($t \to \infty$) is then $A(\infty) = A_{sat} = q$.

For a summary, it is needed to determine NPA which is wanted to measure. For example with statistical error 1% it is 10,000 impulses. Using known cross section, reactor power, detector efficiency and gamma branching ratio the needed irradiation time can be estimated.

6. Validation of ^{90}Zr(n,2n) cross section

Zirconium is an important material used in most of reactor concepts for fuel cladding. Thus the knowledge of its cross section is important for reliable prediction of fuel operation. ^{90}Zr(n,2n) reaction is also included in IRDFF files as dosimetry cross section standard. Due to its very high threshold, 12.1 MeV, it is suitable for measurement of high energy neutrons. One of possible interesting applications is also evaluation of prompt fission neutron spectra in ^{235}U and ^{238}U what is under auspices of the International Atomic Energy Agency in CIELO project.

6.1 Experimental setup

The studied zirconium sample was in the form of encapsulated ZrO_2. This form was chosen thanks to its readily available form of zirconium. Other advantages of this choice includes the suitable neutron properties of oxygen (low absorption and scattering) in aluminum can. These favorable properties are reflected by the small calculated self-shielding correction factor. The aluminum capsule had the inner diameter 8 cm and the external diameter 8.2 cm, which is approximately the same diameter as HPGe detector.
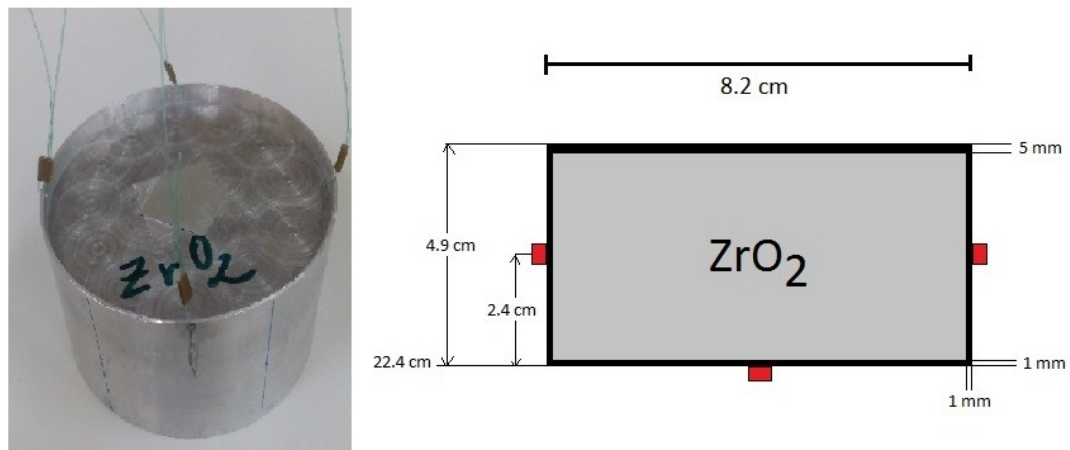

Figure 6.1: The photo (left) and the scheme of ZrO_2 capsule with the activation foils positions (red rectangles).

The sample was placed into the LR-0 reactor core in the dry channel, in the center (see the Figure 6.3 with axial view - the overhead view is the same as in case of MnO_2 and NaI (Figure 7.2)) and was irradiated 5.5 hours at power 5 W with the critical height of the moderator 56.2 cm. The relative power evolution is plotted in the Figure 6.2. The bottom of Zr capsule was placed in 22.4 cm above the zero fuel level.

The activation foils were located in the defined positions on the outer surface capsule – radially symmetric positions (Au in 60° symmetry and Ni in 120° sym-
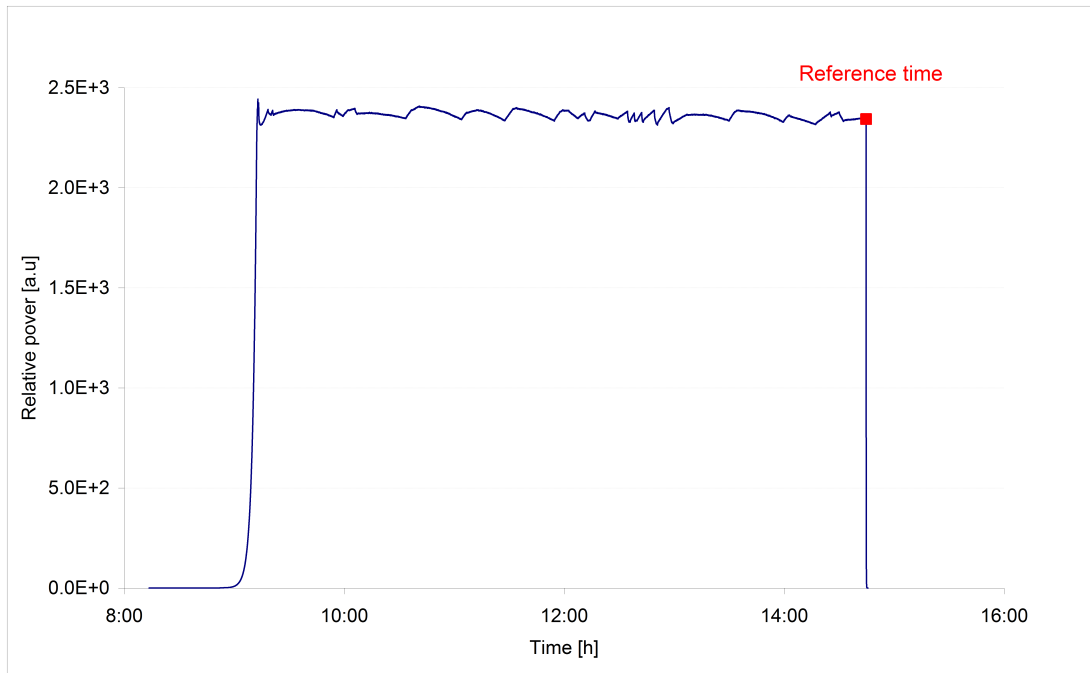
Figure 6.2: Reactor power during the ZrO_2 capsule irradiation. [18]

metry). Foils of Au and Ni were placed in the middle of bottom and around the capsule (2.4 cm above the capsule bottom), see the Figure 6.1. The thickness of the capsule bottom was 1 mm and the cap was 5 mm thick. The density of ZrO_2 in the capsule was 0.773 g/cm^3 and weight was 162.43 g. A set of 1% Au and 100% Ni foils were used for both relative measurement of reaction rate gradient and flux monitoring.
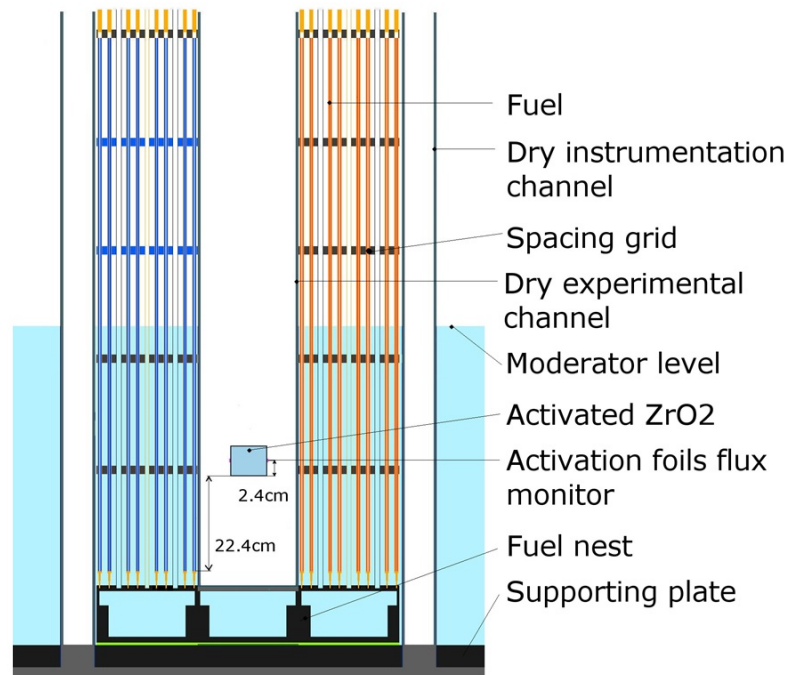

Figure 6.3: Axial view of the core with ZrO_2 capsule position. [18]

28

6.2 Spectrometry of Zr

Gamma spectrometry was used to determine capsule activity by Net Peak Area (NPA). This NPA of photons accompanying decay were measured using a semiconductor HPGe detector placed in a lead shielding with a thin inner copper lining covered with rubber for suppression of a background signal. The capsule was measured directly at the top face of the detector (the detector diameter is approximately equal to capsule diameter), see the Figure 6.4. The ZrO_2 volume was discretized for Coincidence Summing Correction Factor (CSCF). The peak of ^{89}Zr (909.2 keV) might be in coincidence with 511 keV peak, because ^{89}Zr disintegrates by emission of positron. This correction factor was calculated by equation [19]

$$k_{CSCF} = 1 - 2I_{\beta^+} \times \eta_T^{511keV},\tag{6.1}$$

where η_T^{511keV} is the total efficiency for 511 keV peak and I_{β^+} is the positron branching ratio. For the application of the point source geometry formula, the source was discretized into 0.5 cm thick rings which can be assumed as nearly a point source. This assumption can be done because the correction factor using precise evaluation is 0.961, while the approximate solution using point source formula for the volume source gives 0.969.
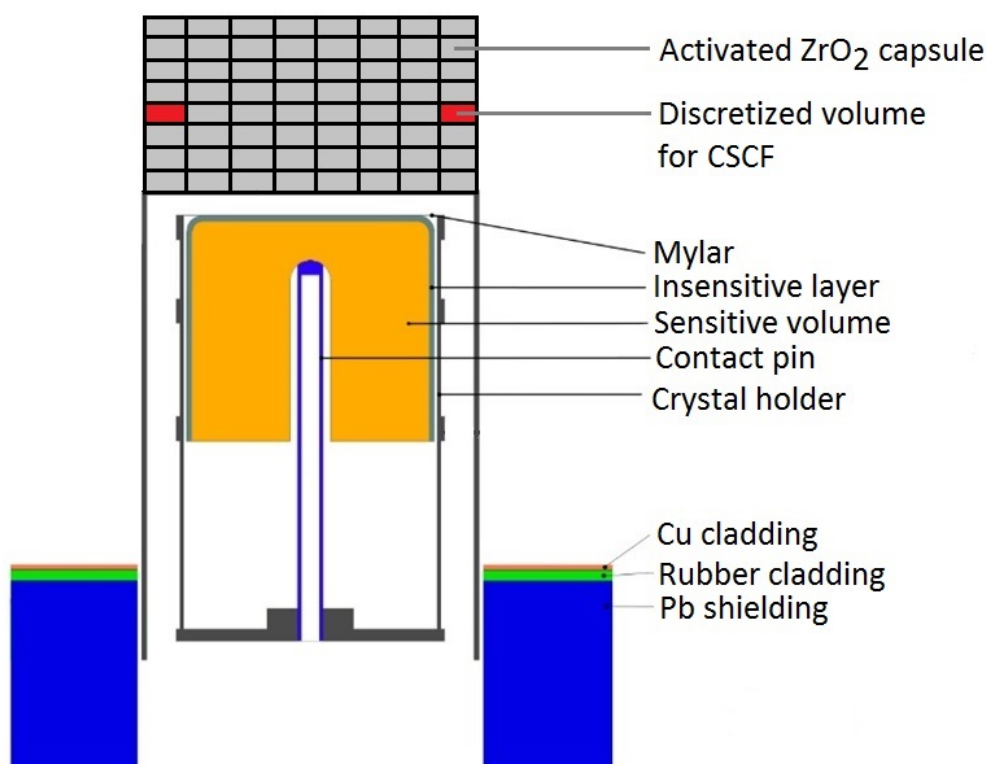

Figure 6.4: The scheme of HPGe detector with irradiated capsule at the end cup and with the scheme of detector shielding. [18]

The HPGe detector efficiency calibration was calculated by MCNP6 code. The computing model of the detector was compiled using experimentally determined

parameters of the detector, which were measured from the detector radiogram and precisely measured insensitive layer, see the Chapter 4 on page 22.

The detector model was verified with the point etalon and Marinelli beaker sources. The discrepancy between calculation and experiment on the front of the detector in relevant gamma energy region is about 1.9% in the point source, which is identical with foils measurement and 1% in Marinelli beaker geometry, which is close to the capsule measurement. The energy calibration was performed using the standard point sources ^{60}Co, ^{88}Y, ^{137}Cs, ^{152}Eu and ^{241}Am with an uncertainty less than 1.0 keV throughout the energy range used, as shown in the Figure 6.5.
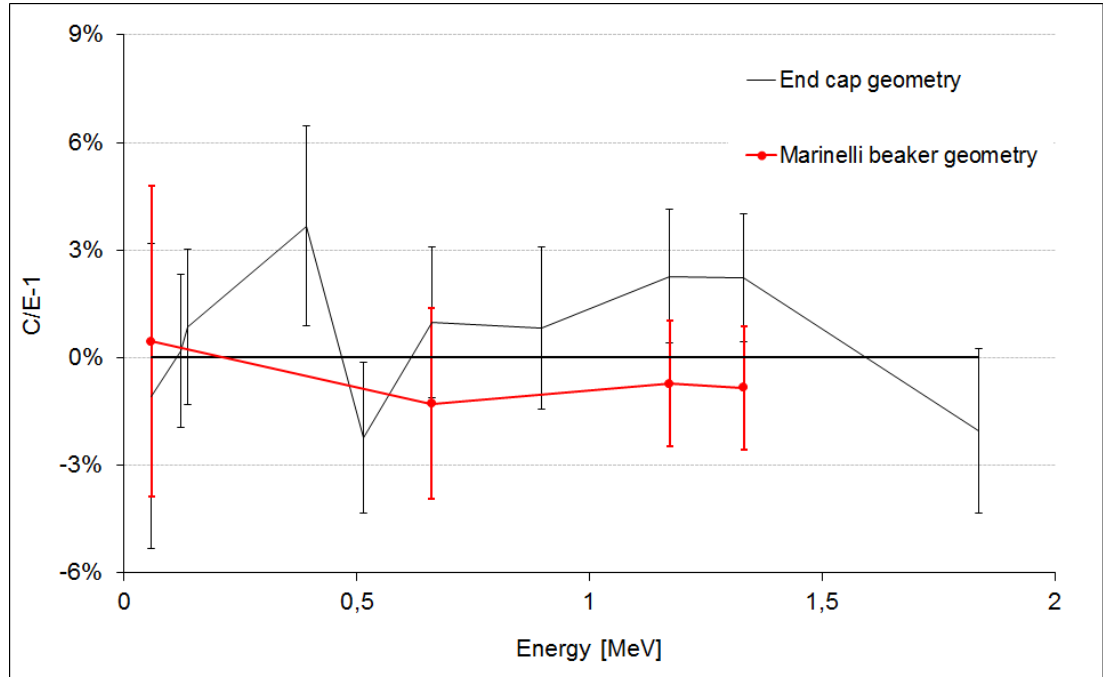
Figure 6.5: Validation of used HPGe detector in both measured geometries. [18]

The obtained photon spectrum was analyzed by Genie 2000 software (Canberra). More information about energy calibration and measurement with this program can by found in [12] and in [13]. This program analysis required peaks and calculated their NPA. In the spectrum of irradiated ZrO_2 sample (see the Figure 6.6) zirconium impurities were observed, namely hafnium. The evaluation of Hf contamination was based on activity of ^{181}Hf, because of high gamma activity k_{CSCF} is close to 1. Based on the gamma spectroscopy, it was determined that the hafnium concentration in sample was about 800 ppm. It is worth noting that for purposes of utilization of zirconium as a fuel cladding, the Hf content is reduced because of the high neutron absorption. In the case of LR-0 the concentration of hafnium in fuel cladding is about 300 ppm. Parameters of measured nuclides are listed in the Table 6.1.

The uncertainty of count rates, which makes at most 1.3% includes the following main components: the gross peak area, the Compton continuum area, the background area and the parameters in the energy and peak shape calibrations. The detector efficiency uncertainty, being about 1% for volume source and about 1.9% for point source, covers statistical uncertainty of gamma transport from source to HPGe, uncertainty in Marinelli beaker position and uncertainty
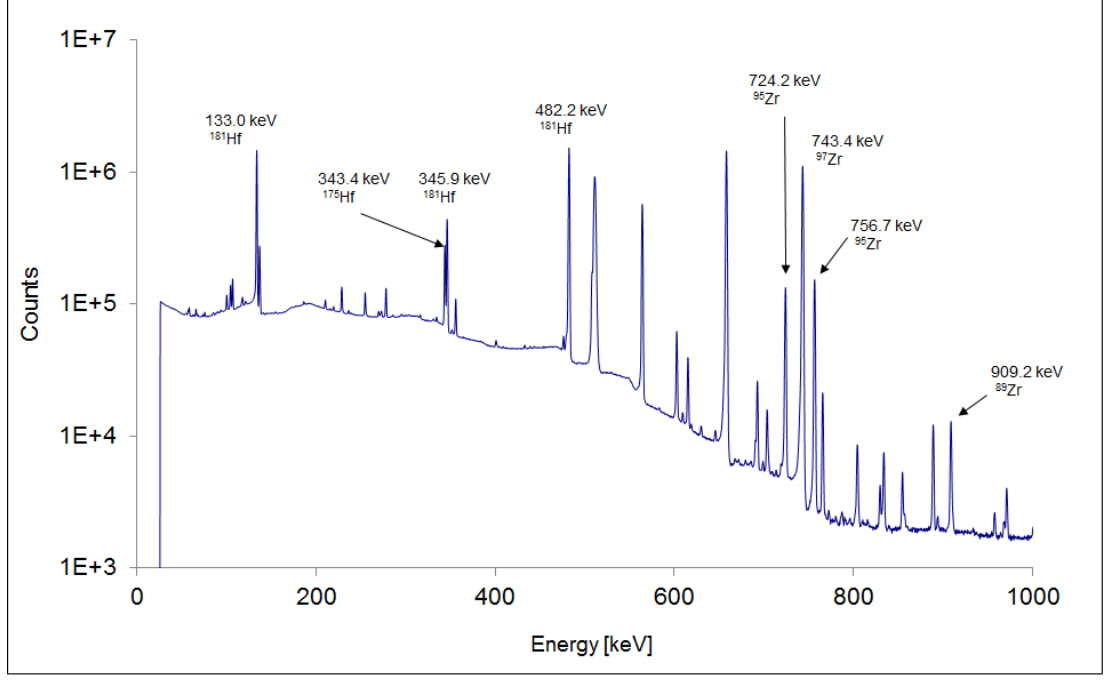
Figure 6.6: HPGe gamma spectrum of irradiated ZrO_2 sample (2 days after irradiation). [18]

Reaction	^{90}Zr(n,2n)
Gamma line energy [keV]	909.2
Detector efficiency	1.25E-02
Branching ratio [%]	99.04
A/A_{sat}	4.81E-02
$T_{1/2}$	78.41 h
k_{CSCF}	0.961

Table 6.1: The summary of gamma peaks used for irradiated sample evaluation.

of source distribution in volume source is determined as bias between calculated and experimentally determined efficiency. Besides the above stated uncertainties, there are also other stochastic uncertainties: The radionuclide half live value, the pin radial or axial position data determination and the reactor shut-down time uncertainties. However, these uncertainties are negligible in comparison with the count rate uncertainties. The reaction rate during irradiation was determined by the equation

$$q = \left[\frac{A(\overline{P})}{A_{sat}(\overline{P})}\right]^{-1} C(T_{live}) \frac{\lambda}{\epsilon \eta N} \frac{1}{(1 - e^{-\lambda T_{live}})} \frac{1}{e^{-\lambda \Delta T}} \frac{1}{k_{CSCF}}, \quad (6.2)$$

where $\frac{A(\overline{P})}{A_{sat}(\overline{P})} = \sum P_{rel}^i (1 - e^{-\lambda T_{irr}^i}) e^{-\lambda T_{end}^i}$ is relative portion of saturated activity induced during irradiation experiment, P_{rel}^i is the relative power in i-th interval of the irradiation period ($P_{rel}^i = \frac{P^i}{\overline{P}}$), T_{irr}^i is irradiation time in i-th interval of the irradiation period, T_{end}^i is the time from the end of i-th irradiation interval

to the reference time (end of irradiation period), λ is the decay constant, $\overline{P}$ is the mean power, T_{live} is live time of measurement by HPGe detector, ΔT is the time between the end of irradiation and the start of HPGe detector measurement, $C(T_{live})$ is the measured number of counts $\left(C(T_{live}) = \frac{NPA}{t_{live}} \right)$, ϵ is the gamma branching ratio, η is the HPGe detector efficiency (MCNP6 calculations), N is the number of target isotope nuclei and k_{CSCF} is coincidence summing correction factor.

It was proven by measurement that the other channel, namely ^{90}Zr(γ,n) in case of ^{89}Zr does not significantly contribute to the observed production rate because the concurrent reactions have a high threshold and low cross sections.

6.3 Normalization of neutron flux by activation foils and MCNP6 calculations

The integral cross sections are derived from the reaction rates of the samples scaled to unit neutron emission rate. The scaling factors normalizing measurement to actual irradiation power, used in evaluation of ^{90}Zr(n,2n) reaction rate, have been determined by reaction rates derived from gamma activity of activation foils. Two kinds of foils were used: 1% Au in Al and 100% Ni. Foils were cylindrical with 3.6 mm diameter and thickness of 0.1 mm. Irradiated activation foil was placed in a plastic cover of EG3 point source type – outer diameter 25 mm and inner diameter 4 mm and also measured at the end cup the HPGe detector (see the Figure 6.7). For Au foils the spectrum was evaluated for the 411.8 keV peak of ^{198}Au originating from the ^{197}Au(n,γ) reaction and for Ni foil the spectrum was evaluated for the 810.8 keV peak of ^{58}Co originating from the ^{58}Ni(n,p) reaction. Foils parameters are summarized in the Table 6.2. The foils measurement started immediately after the end of irradiation and the self-absorption in foils and the geometry corrections were negligible as well as the dead time correction. The NPA was also corrected to CSCF.
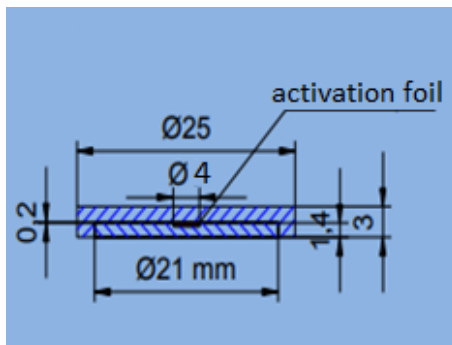

Figure 6.7: The scheme of activation foils capsule.

The reaction rates for foils were also calculated by the equation 6.2. The experimental reaction rate of the studied (n,2n) reactions were scaled to unit neutron emission in the core using the scaling factor K derived from the monitoring activation foils. The scaling factor K (number of neutrons in the reactor core) was determined from the comparison of calculated (to one neutron per second in

Activation material	^{198}**Au**	^{58}**Co**
Reaction	^{197}Au(n,γ)	^{58}Ni(n,p)
Gamma line energy [keV]	411.8	810.8
Branching ratio [%]	95.62	99.45
$T_{1/2}$ [days]	2.6947	70.86
A/A_{sat}	5.80E-02	2.26E-03
Detector efficiency	8.30E-02	4.63E-02
Derived reaction rate [1/s]	4.18E-15	2.52E-18
k_{CSCF}	0.998	0.936
K	3.72E+11	3.92E+11

Table 6.2: Summary of activation detector parameters.

reactor core - 1 nps) and measured reaction rates of the activation foils. The average scaling factor, used for absolute neutron flux evaluation, is approximately 3.82E+11 and was determined by the equation

$$K = \frac{K_{Au} + K_{Ni}}{2}, \tag{6.3}$$

where $K_{Au} = \sum_{i=1}^{N} \frac{q_{Au}^i(1\,nps)_{Calculated}}{q_{Au}^i(\overline{P})_{Measured}}$ is the scaling factor determined from the Au reaction rates and $K_{Ni} = \sum_{i=1}^{N} \frac{q_{Ni}^i(1\,nps)_{Calculated}}{q_{Ni}^i(\overline{P})_{Measured}}$ is the scaling factor determined from Ni reaction rates. The assumed uncertainty in determined scaling factor is about 3.7%.

In MCNP6 was, with the reaction rate, also calculated the relative flux in the reactor core ($\phi_{rel}(1\,nps)$). For the correctness of the calculations, a well-defined reactor spectrum is needed. Several experiments have been carried out to confirm the accuracy of the MCNP6 model (see the Chapter 3 on page 12).

The simulations of neutron and photon transport were performed in criticality calculations using MCNP6 Monte Carlo code and ENDF-VII/CIELO data library - ^{235}U prompt fission neutron spectra (PFNS) was calculated by ENDF-VII and CIELO nuclear data libraries. Simulation of gamma transport from the sample to the HPGe detector was determined with a single gamma transport model. Simulation of target activation caused by neutron transport was determined in MCNP6 model. More details about calculations can be found in [18].

6.4 Self shielding correction factor

The self shielding factor is described by the difference between the ^{235}U fission spectrum and the spectrum in the activation detector (capsule). This factor can be divided into two components. First is spectral shift effect caused by the difference between the pure spectrum of ^{235}U and real spectrum in the reactor. The reactor has not only the ^{235}U spectrum, but also the spectrum of ^{238}U and delayed neutrons. In LR-0 reactor is no other effects as is fuel burning because it is a zero power reactor. In this case, this spectral shift effect correction is close to 1, because the fission spectrum of ^{235}U and LR-0 reactor spectrum above 6 MeV

are close, and thus the reactor spectrum can be approximately considered as a clear spectrum of ^{235}U for measurement of spectral average cross-sections with a threshold above 10 MeV, see the Figure 3.9.

The second is the spectral shift effect caused by the difference between the spectrum in activation detector (capsule) and the reactor spectrum. If the capsule has good neutron properties, the spectrum is not shifted but only attenuated. Then it is called flux loss effect, where the neutrons are absorbed by the sample or reflected. The effect of neutron flux attenuation in ZrO_2 target can be seen in the Figure 6.8. For low neutron energy, the flux loss changes, but for neutron energy greater then 10 MeV, the flux loss is approximately consistent and in this case is 6.2%.
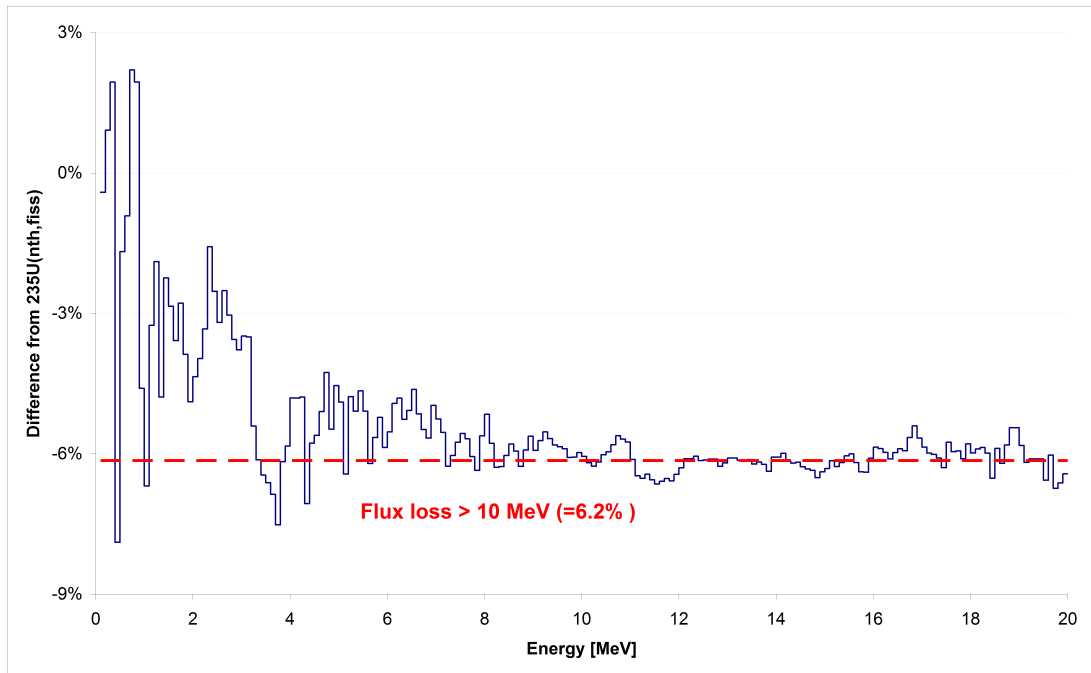
Figure 6.8: The effect of neutron flux attenuation in ZrO_2 target. [18]

6.5 Final results

The resulting neutron flux Φ is obtained by multiplying calculated relative flux $\phi_{rel}(1\,nps)$ with the scaling factor K and the resulting value of the spectral average cross-section (SACS) is then given by the equation

$$\overline{\sigma} = \frac{q}{K \times \int_{E>10\,MeV} \phi(E)dE} \times C \qquad (6.4)$$

where q is measured reaction rate of ZrO_2 capsule from equation 6.2 and C is the self shielding correction factor.

The summary of measured results are in the Table 6.3. The components of the total uncertainty are listed in the Table 6.4. Since the sources of uncertainties are assumed as not-correlated, the total uncertainty is derived as square root of the sum of the squares of all combined uncertainties.

In the Table 6.5 are calculated values of spectral average cross-section from various libraries and the comparison of calculated reaction rates with measured result (C/E-1). In this table, the difference between the results with PFNS of ^{235}U from CIELO and from ENDF-VII nuclear data libraries, can be seen. CIELO has a less notable discrepancies.

The cross-sections of ^{90}Zr(n,2n) reaction in various libraries are in the Figure 6.9.

	^{90}Zr(n,2n)
A [Bq]	47.91
q [s^{-1}]	2.40E-21
Neutron emission rate [s^{-1}]	3.82E+11
Correction to spectral shift	0.999
Correction to flux loss	6.2%
SACS in reactor spectra $> 10\,$MeV [mb]	76.8
Cross-section in ^{235}U [mb]	**0.107**
Uncertainty	**3.88**%

Table 6.3: Results of ZrO$_2$ measurement.

	^{90}Zr(n,2n)
Statistical uncertainty in gamma spectrometry measurement	1.3%
Statistical uncertainty in Au foils measurement	0.6%
Statistical uncertainty in Ni foils measurement	0.7%
Bias between Au and Ni foils based scaling factors	2.5%
Uncertainty in self shielding correction	1.3%
Uncertainty in HPGe description for samples	1%
Uncertainty in HPGe description for activation foils measurement	1.9%
Total uncertainty	3.88%

Table 6.4: Uncertainties of ZrO$_2$ measurement.

	^{90}Zr(n,2n)			
	Calculated q [s^{-1}] (ENDF-VII)	C/E-1	Calculated q [s^{-1}] (CIELO)	C/E-1
ENDF VII.1	5.54E-33	-11.9%	6.24E-33	-0.7%
ENDF VII	5.62E-33	-10.7%	6.32E-33	0.4%
JEFF 3.2	5.85E-33	-7.0%	6.57E-33	4.4%
JEFF 3.1	5.54E-33	-12.0%	6.22E-33	-1.0%
JENDL 3.3	5.85E-33	-7.0%	6.57E-33	4.4%
JENDL 4	5.85E-33	-7.0%	6.57E-33	4.4%
ROSFOND	5.43E-33	-13.7%	6.12E-33	-2.7%
CENDL 3.1	5.85E-33	-7.0%	6.57E-33	4.4%
IRDFF	5.51E-33	-12.4%	6.20E-33	-1.4%
Uncertainty	1.4%	4.13%	1.7%	4.23%

Table 6.5: Calculation and C/E-1 comparison with ^{90}Zr(n,2n) reaction rate experimental data. [14] [15] [21] [22] [23] [24] [25] [26] [27]
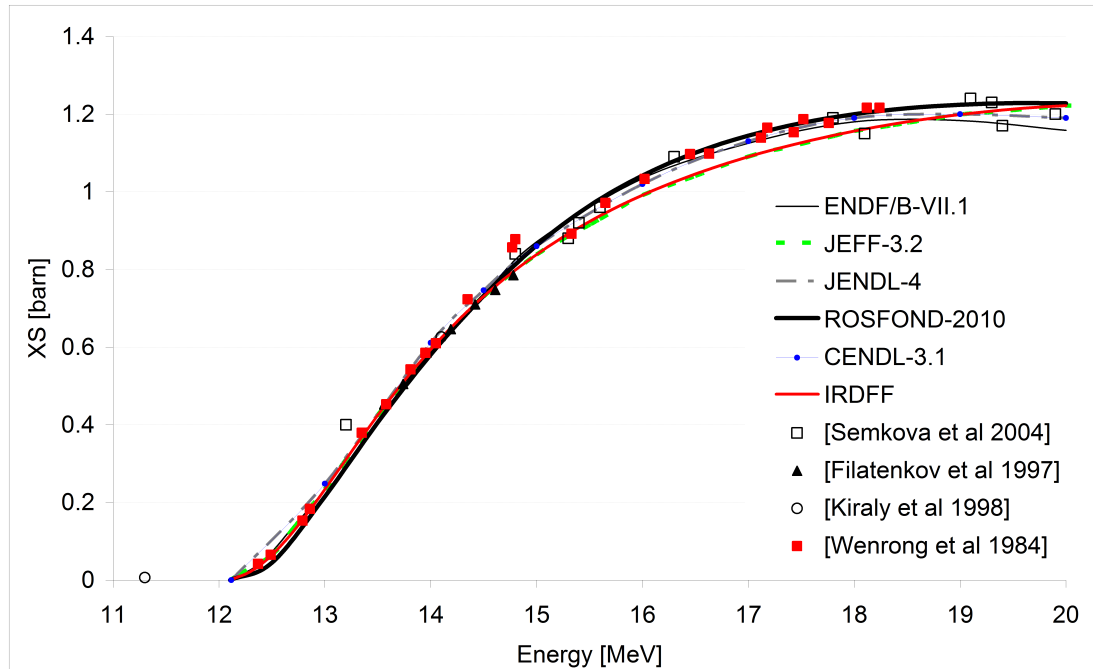
Figure 6.9: Cross-sections of ^{90}Zr(n,2n) reaction in various libraries together with some available EXFOR data. [18]

7. Validation of ^{55}Mn(n,2n) and ^{127}I(n,2n) cross sections

This experiment is similar to the previous measurement of spectral average cross-section of ^{90}Zr(n,2n) reaction and thus will be described shortly.

7.1 Experimental setup

The studied ^{55}Mn and ^{127}I were in the form of encapsulated MnO_2 and NaI. In this case the both two capsules were placed in LR-0 core in dry channel in the center together. MnO_2 and NaI were fed into the aluminum capsules with inner diameter 8 cm and external diameter 8.2 cm as Zr in previous experiment (see the Figure 7.3). In the Table 7.1 are summarized properties and dimensions data of the both capsules.

	MnO_2	NaI
Bottom thickness [mm]	3	3
Cap thickness [mm]	1.5	1.5
Density [g/cm^3]	1.626	2.144
Weight [g]	99.68	143.32
Height of sample in capsule [mm]	12.2	13.3

Table 7.1: Properties and dimensions of irradiated capsules.

The bottom of capsules was placed also in 22.4 cm above the zero fuel level. The irradiation was carried out 13 hours (7 hours first day and 6 hours second day of irradiation). The relative power evolution is plotted in the Figure 7.1. Reference time for subsequently evaluation was chosen as the end of irradiation the second day.

The critical height of the moderator during this experiment was 56.06 cm during the first day of irradiation and 56.09 cm during the second day. The overhead view of capsules in the LR-0 reactor core with photo is in the Figure 7.2, where the power monitoring channels positions are indicated by round circles around the core, the distances of these eight dry channels to the closest fuel pin, which are measured perpendicularly to the fuel assembly wall, are indicated by subscripts "a" to "l" and the fuel enrichment for each assembly can be also seen in the Figure 7.2. The axial view is the same as in the case of Zr irradiation (6.3).

The activation foils were also located in the defined positions on the outer surface of both capsules – radially symmetric positions (Au in 60° symmetry and Ni in 120° symmetry). Monitoring foils of Au and Ni were placed in the middle of bottom and around both capsules (1.15 cm above the capsule bottom at MnO_2 and 3.2 cm above the bottom at NaI capsule), see the Figure 7.3.
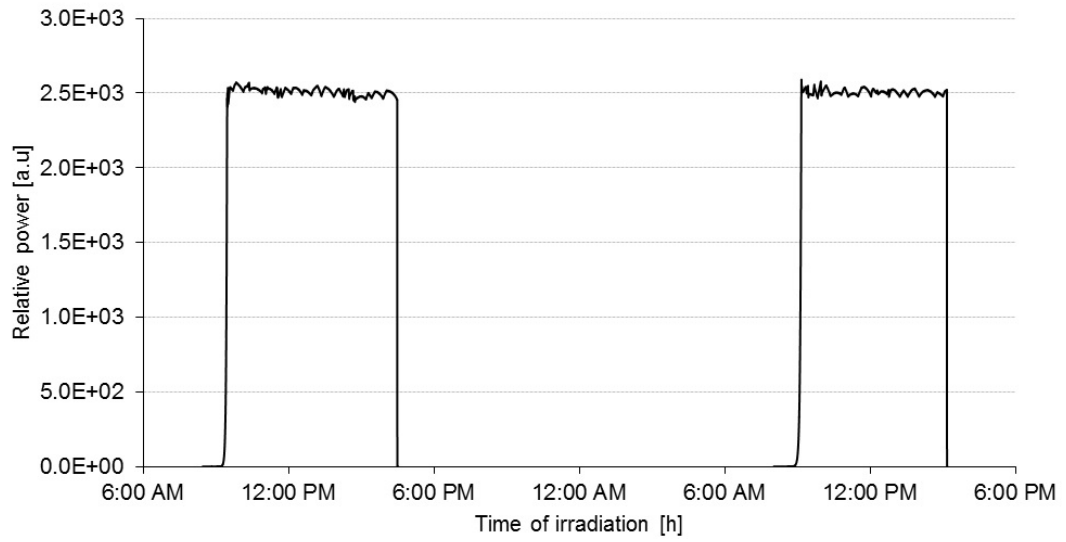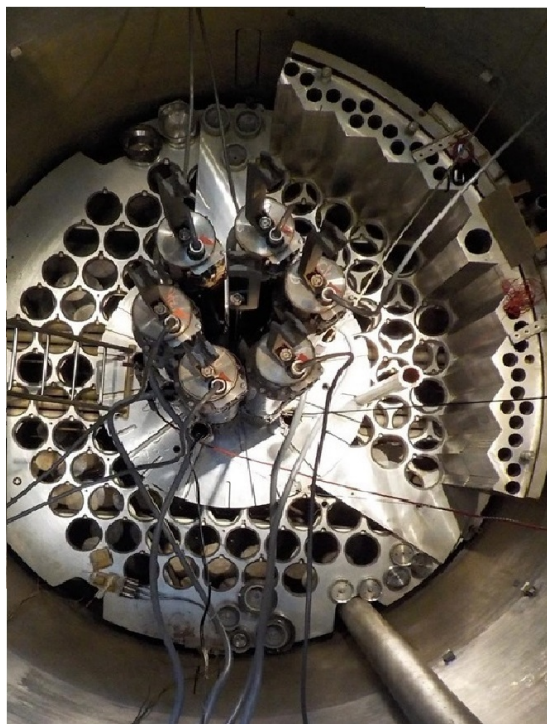
Figure 7.1: Reactor power during the irradiation. [20]
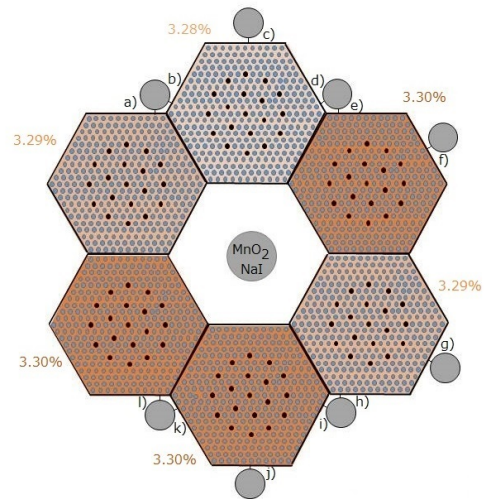
a) 1mm	e) 1mm	i) 2mm
b) 1mm	f) 6mm	j) 6mm
c) 6mm	g) 7mm	k) 11mm
d) 2mm	h) 1mm	l) 2mm

Figure 7.2: Overhead view at LR-0 reactor core (left) and radial plot of the core with position of irradiated sample (right). [20]

	MnO$_2$	**NaI**	
Gamma line energy [keV]	834.8	388.6	666.3
Detector efficiency	1.80E-02	2.94E-02	2.01E-02
Branching ratio [%]	99.98	35.60	32.90
A/A$_{sat}$	1.21E-03	2.83E-02	
T$_{1/2}$ [d]	312.20	12.93	
k$_{CSCF}$	1	0.997	

Table 7.2: Parameters of measured gamma peaks from irradiated capsules.
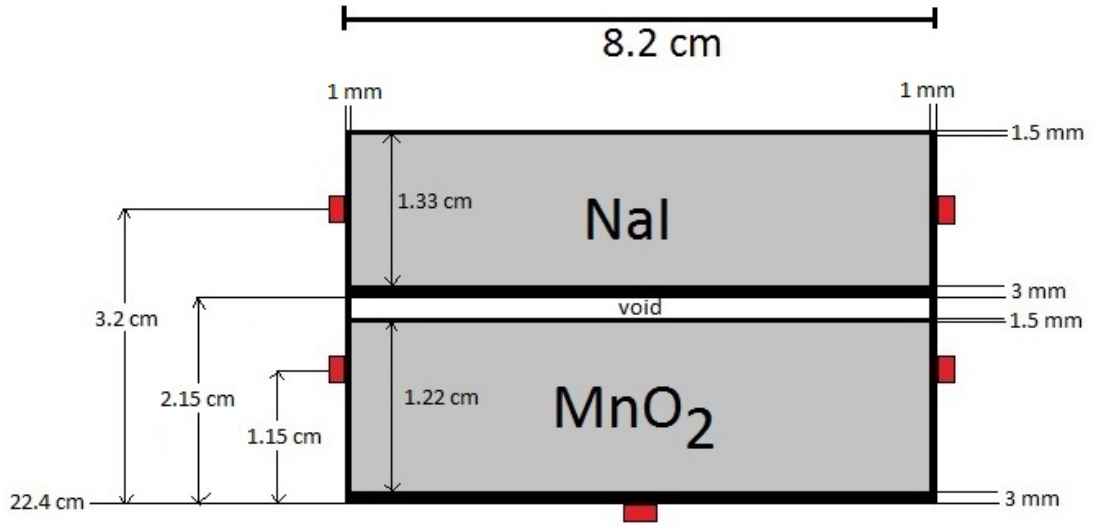
Figure 7.3: The scheme of MnO$_2$ and NaI capsules with the activation foils positions (red rectangles). [20]

7.2 HPGe spectrometry

For this measurement, the same HPGe detector was used as in the case of Zr measurement. Both capsules were measured directly at the top face of detector. In case of MnO$_2$ capsule, the k_{CSCF} is 1 (there is no Coincidence Summing Factor) and in the case of NaI capsule, the volume was discretized like ZrO$_2$ capsule. The measured part of spectrum of MnO$_2$ capsule can be seen in the Figure 7.4 and the measured part of spectrum of NaI is in the Figure 7.5. The parameters of measured gamma peaks are summarized in the Table 7.2.

The reaction rates were determined from the equation 6.2. Normalization of neutron flux by means of activation foils were the same as in the case of Zr measurement. The average scaling factor K was same for the both capsules and was approximately 4.20E+11. The assumed uncertainty in scaling factor is about 3.5%. The parameters of measured foils are summarized in the Table 7.3.
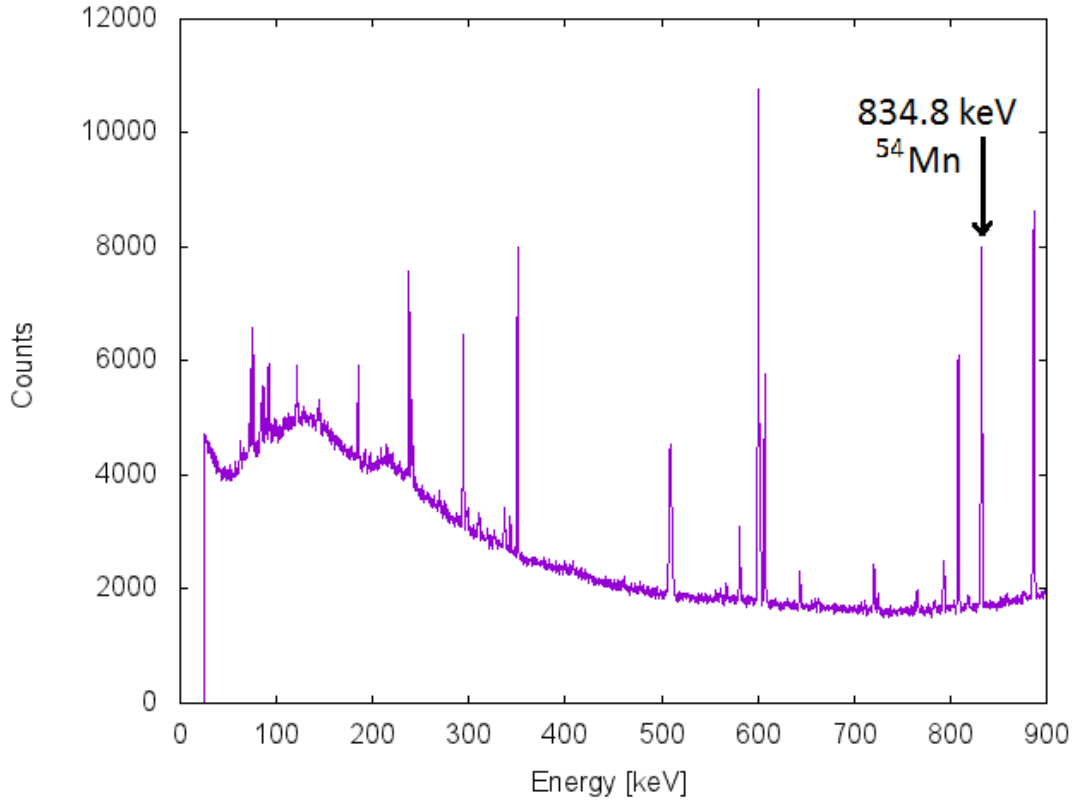
Figure 7.4: Part of HPGe gamma spectrum of irradiated MnO_2 sample.

7.3 Final results

The resulting values of the spectral average cross sections were calculated also by the equation 6.4, where q is the measured reaction rate of MnO_2 and NaI capsules. The summary of measured results are in the Table 7.4 and the components of the total uncertainty are listed in the Table 7.5. Table 7.6 shows the differences between calculated values of spectral average cross-section from various libraries (with PFNS of ^{235}U from ENDF-VII library) and measured results.

Notable discrepancies were found in the ^{127}I(n,2n) cross section. JENDL 3.3 and JENDL 4 over predict the result by about 31.3%. This big difference between calculated results in these libraries and measured result can be caused by two factors. The spectral average cross-section in the library can be wrong or PFNS in ENDF-VII library is wrong. As can be seen in the ^{90}Zr(n,2n) reaction result (Figure 6.5), the PFNS from CIELO nuclear data library has less discrepancies. It means that CIELO has more accurate PFNS of ^{235}U in high energy region. Discrepancies in case of CIELO calculations shows that also cross-sections of selected reactions can be wrong in nuclear data libraries.

ROSFOND, ENDF VII and ENDF VII.1 results differ from experiment by 2%. Less discrepancies were found in ^{55}Mn(n,2n) cross section, where greatest discrepancy is in the IRDFF nuclear library.

The cross-sections of ^{55}Mn(n,2n) reaction in various libraries are in the Figure 7.6 and of ^{127}I(n,2n) reaction are in the Figure 7.7.

40
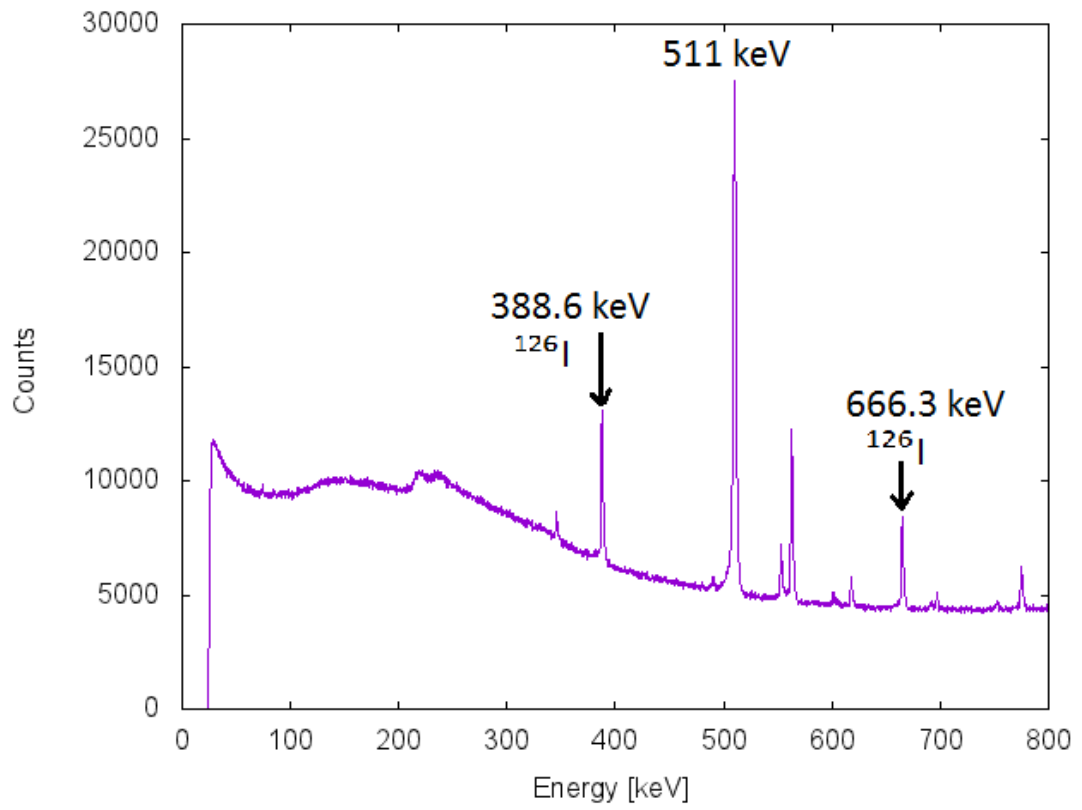
Figure 7.5: Part of HPGe gamma spectrum of irradiated NaI sample.
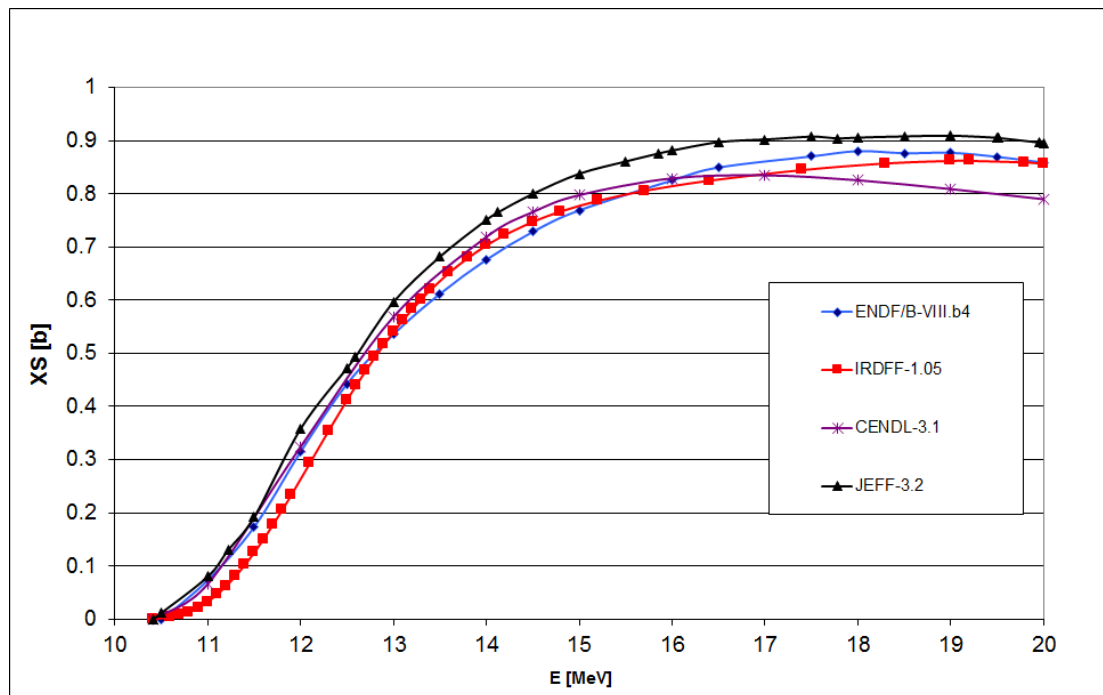
Figure 7.6: Cross-sections of ^{55}Mn(n,2n) reaction in various libraries.

Activation material	^{198}**Au**	^{58}**Co**
Reaction	^{197}Au(n,γ)	^{58}Ni(n,p)
Gamma line energy [keV]	411.8	810.8
Branching ratio [%]	95.62	99.45
$T_{1/2}$ [days]	2.6947	70.86
A/A_{sat}	1.20E-01	5.31E-03
Detector efficiency	8.30E-02	4.63E-02
Derived reaction rate	4.43E-15	2.79E-18
k_{CSCF}	0.998	0.936
K	4.05E+11	4.37E+11

Table 7.3: Summary of activation detector parameters.

	^{55}**Mn(n,2n)**	^{127}**I(n,2n)**
A [Bq]	8.0465	453.8715
q [s^{-1}]	5.13E-21	2.78E-20
Neutron emission rate [s^{-1}]	4.2E+11	
Correction to spectral shift	0.954	0.991
Correction to flux loss	10.3%	6.6%
SACS in reactor spectra > 10 MeV [mb]	163.6019	858.4357
Cross-section in ^{235}U [mb]	**0.2393**	**1.2087**
Uncertainty	**4.21**%	**4.36**%

Table 7.4: Results of MnO$_2$ and NaI measurements.

	^{55}**Mn(n,2n)**	^{127}**I(n,2n)**
Statistical uncertainty in gamma spectrometry measurement	1.02%	1.10%
Bias between evaluated peaks	-	1.06%
Statistical uncertainty in Au foils measurement	1.13%	
Statistical uncertainty in Ni foils measurement	1.75%	
Bias between Au and Ni foils based scaling factors	2.6%	
Uncertainty in self shielding correction	1%	
Uncertainty in HPGe description for samples (Figure 6.5)	1%	
Uncertainty in HPGe description for activation foils measurement	1.9%	
Total uncertainty	4.21%	4.36%

Table 7.5: Uncertainties of MnO$_2$ and NaI measurements.

	^{55}Mn(n,2n)		^{127}I(n,2n)	
	Calculated q [s^{-1}] (ENDF-VII)	C/E-1	Calculated q [s^{-1}] (ENDF-VII)	C/E-1
ENDF VII.1	5.13E-21	0.1%	2.73E-20	-2.0%
ENDF VII	4.93E-21	-3.9%	2.73E-20	-2.0%
JEFF 3.2	5.48E-21	6.8%	2.97E-20	6.6%
JEFF 3.1	5.13E-21	0.1%	2.97E-20	6.6%
JENDL 3.3	5.13E-21	0.1%	3.66E-20	31.3%
JENDL 4	5.13E-21	0.1%	3.66E-20	31.3%
ROSFOND	5.13E-21	0.1%	2.73E-20	-2.0%
CENDL 3.1	5.13E-21	0.1%	3.09E-20	11.1%
IRDFF	4.32E-21	-15.8%	2.69E-20	-3.5%
Uncertainty	2.99%	5.2%	1.94%	4.8%

Table 7.6: Calculation and C/E-1 comparison with ^{55}Mn(n,2n) and ^{127}I(n,2n) reaction rate experimental data.
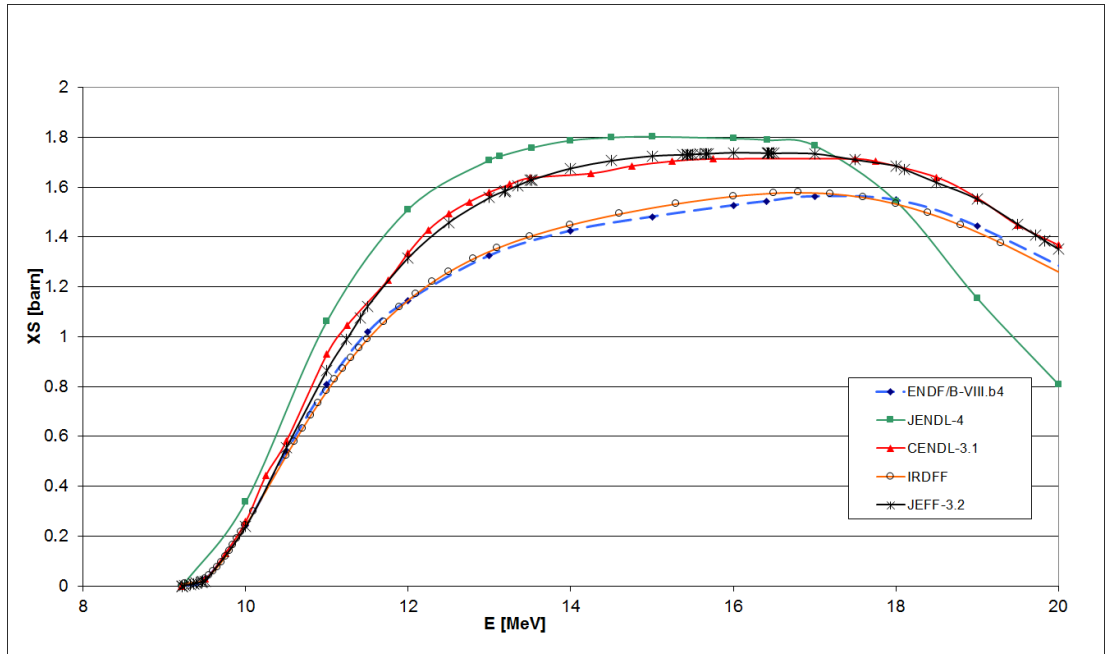
Figure 7.7: Cross-sections of ^{127}I(n,2n) reaction in various libraries.

Conclusion

In this thesis the spectral average cross-sections of ^{55}Mn(n,2n), ^{127}I(n,2n) and ^{90}Zr(n,2n) reactions were measured. The results are summarized in the Table 7.7. The similar measurements of the same reactions were also performed by W. Mannhart and K. Zolotarev. For the ^{90}Zr(n,2n) reaction, W. Mannhart presents as a result 0.1027 mb [28] with uncertainty 2.67%. In the case of ^{127}I(n,2n) reaction, W. Mannhart presents the result 1.279 mb [28] with uncertainty 3.37%, while K. Zolotarev presents the result 1.197 mb [28] with uncertainty 3.43%, which is more close to result presented here. In the case of ^{55}Mn(n,2n) reaction, our measured result of 0.2393 mb is approximately the same as the result presented by W. Mannhart, 0.236 mb [28] with the uncertainty 2.8%, while the result presented by K. Zolotarev is 0.204 mb [28] with the uncertainty 3.62%.

Validation of SACS is important for the reactor dosimetry and the results are also used for refining the neutron fission spectrum of ^{235}U in the region of higher neutron energies, where there are considerable differences between CIELO and other nuclear data libraries, see the Figure 3.9.

	^{55}Mn(n,2n)	^{127}I(n,2n)	^{90}Zr(n,2n)
A [Bq]	8.0465	453.8715	47.91
q [s^{-1}]	5.13E-21	2.78E-20	2.40E-21
Neutron emission rate [s^{-1}]	4.2E+11		3.82E+11
Correction to spectral shift	0.954	0.991	0.999
Correction to flux loss	10.3%	6.6%	6.2%
SACS in reactor spectra > 10 MeV [mb]	163.6019	858.4357	76.8
Cross-section in ^{235}U [mb]	**0.2393**	**1.2087**	**0.107**
Uncertainty	**4.21**%	**4.36**%	**3.88**%

Table 7.7: Results of MnO$_2$, NaI and ZrO$_2$ measurements.

Bibliography

[1] Capote, R., Trkov, A. (coordinators), (2017): *IAEA CIELO Data Development Project* within the International Pilot Project of the OECD/NEA [1] (see www-nds.iaea.org/CIELO/).

[2] IAEA IRDFF: The IAEA Coordinated Research Projecton Testingand Improving the International Reactor Dosimetry and Fusion File. https://www-nds. iaea.org/IRDFFtest/; [request for new measurements]: https://www-nds.iaea. org/IRDFFtest/HPRL.pdf.

[3] Physics LAB - *Famous Experiments: The Discovery of the Neutron* `http://dev.physicslab.org/Document.aspx?doctype=3&filename= AtomicNuclear_ChadwickNeutron.xml`

[4] Overton, Gail. (2012): *ORGANIC CRYSTALS: Stilbene crystals improve neutron detection.* [online]. `https://www.laserfocusworld.com/articles/print/volume-48/ issue-11/world-news/organic-crystals-stilbene-crystals- improve-neutron-detection.html`

[5] *nuclear-power.net* [online]. `https://www.nuclear-power.net/nuclear-power/reactor-physics /atomic-nuclear-physics/fundamental-particles/neutron/ interactions-neutrons-matter/`

[6] Košťál, M., Schulc, M., Šimon, J., Burianová, N., Harutyunyan, D., Losa, E., Rypar, V. (2018): *Measurement of various monitors reaction rate in a special core at LR-0 reactor.* Annals of Nuclear Energy, Vol. 112, Pp 759-768, ISSN 0306-4549.

[7] Košťál, M., Švadlenková, M., Baroň, P. et al. (2016): *Determining the axial power profile of partly flooded fuel in a compact core assembled in reactor LR-0.* Annals of Nuclear Energy, Vol. 90, pp. 450-458, ISSN 0306-4549.

[8] Košťál, M., Matěj, Z., Cvachovec, F., Rypar, V., Losa, E., Rejchrt, J., Mravec, F., Veškrna, M. (2017): *Measurement and calculation of fast neutron and gamma spectra in well defined cores in LR-0 reactor.* Applied Radiation and Isotopes, Vol. 120, pp 45-50.

[9] Košťál, M., Rypar, V., Milčák, J., Juříček, V., Losa, E., Forget, B., Harper, S. (2016): *Study of graphite reactivity worth on well-defined cores assembled on LR-0 reactor.* Annals of Nuclear Energy, Vol. 87, pp. 601-611, ISSN 0306-4549.

[10] Košťál, M. et al.(2018): *On similarity of various reactor spectra and 235U prompt fission neutron spectrum.* Applied Radiation and Isotopes, Vol. 135, Pp. 83-91.

[11] Rychlecký, Jakub. *Research Centre Řež - Research Reactor LR-0* [online]. `http://cvrez.cz/en/infrastructure/research-reactor-lr-0/`

[12] Burianová, N.(2016): *Gama spektrometrie v reaktorové fyzice na experimentálním reaktoru LR-0 v Řeži.* Bachelor thesis. Faculty of Mathematics and Physics, Charles University, Prague, 72 pages.

[13] CANBERRA Industries (2006): *Genie 2000 3.1 - Customization Tools Manual.* Meriden, CT 06450.

[14] Chadwick, M.B., Obložinský , P., Herman, M., et al., (2006): *ENDF/B-VII.0: next generation evaluated nuclear data library for nuclear science and technology.* Nucl. Data Sheets 107 (12), 2931–3060.

[15] Chadwick, M.B., Herman, M., Obložinský , P., et al., (2011): *ENDF/B-VII.1: nuclear data for science and technology: cross sections, covariances, fission product yields and decay data.* Nucl. Data Sheets 112, 2887–2996.

[16] OECD Nuclear Energy Agency, Collaborative International Evaluated Library Organisation (CIELO) Pilot Project, WPEC Subgroup 40 (SG40) (seewww.oecdnea.org/science/wpec/sg40-cielo/).

[17] Dryak, P., Kovar, P., (2006): *Experimental and MC determination of HPGe detector efficiency in the 40–2754 keV energy range for measuring point source geometry with the source-to-detector distance of 25 cm.* Appl. Rad. Isot. 64 (2006), 1346–1349.

[18] Košťál, M., Schulc, M., Rypar, V., Losa, E., Burianová, N., Šimon, J., Mareček, M., Uhlíř, J. (2017): *Validation of zirconium isotopes (n,g) and (n,2n) cross sections in a comprehensive LR-0 reactor operative parameters set.* Applied Radiation and Isotopes, Vol. 128, Pp 92-100, ISSN 0969-8043.

[19] Richardson, A.E., Sallee, W.W., (1990): *Coincidence summing corrections for positron emitters in germanium gamma spectrometry.* Nucl. Instrum. Methods Phys. Res. A, Vol. 299, pp. 344–348.

[20] Burianová, N.,Košťál, M., Schulc, M., Šimon, J., Mareček, M., Uhlíř, J. (2018): *Validation of 55Mn(n,2n) and 127I(n,2n) LWR spectrum averaged differential cross sections.* Will be published.

[21] Koning, A.J. et al. (2010): *Status of the JEFF Nuclear Data Library.* Proceedings of the International Conference on Nuclear Data for Science and Technology, Jeju Island, Korea, p.1057

[22] Koning, A.J., Forrest, R., Kellett, M., et al., (2006): *The JEFF-3.1 Nuclear Library.* JEFF Report 21, NEA No. 6190.

[23] Shibata, K., Kawano, T., Nakagawa, T., et al., (2002): *Japanese evaluated nuclear data library version 3 revision-3: JENDL-3.3.* J. Nucl. Sci. Technol. 39, 1125.

[24] Shibata, K., Iwamoto, O., Nakagawa, T., Iwamoto, N., Ichihara, A., Kunieda, S., Chiba, S., Furutaka, K., Otuka, N., Ohsawa, T., Murata, T.,

Matsunobu, H., Zukeran, A., Kamada, S., Katakura, J., (2011): *JENDL-4.0: a new library for nuclear science and engineering.* J. Nucl. Sci. Technol. 48, 1–30.

[25] Zabrodskaya, S., Ignatyuk, a., Kosheev, V., Nikolaev, M., Pronyaev, V.(2007): *ROSFOND – Russian national library of neutron data VANT (Voprosi Atomnoy Nauki i Techniki).* Ser. Nucl. Const., 1–2, pp. 3–21

[26] Ge, Z.G., Zhuang, Y.X., Liu, T.J., Zhang, J.S., Wu, H.C., Zhao, Z.X., Xia, H.H., (2010): *The Updated Version of Chinese Evaluated Nuclear Data Library (CENDL-3.1).* In: Proc. International Conference on Nuclear Data for Science and Technology, Jeju Island, Korea (April 2010), pp. 26–30.

[27] Capote, R., Zolotarev, K.I., Pronyaev, V.G., Trkov, A., (2012): *Updating and extending the IRDFF-2002 dosimetry Library.* J. ASTM Int. (JAI) 9 (4). JAI104119.

[28] IAEA, (2015): https://www-nds.iaea.org/IRDFFtest/SPA_Exp_U235.pdf

List of Figures

List of Tables

List of Abbreviations

Chinese Evaluated Nuclear Data Library	CENDL
Coincidence summing correction factor	CSCF
Collaborative International Evaluated Library Organization	CIELO
Cross-section	XS
Experimental light water reactor in Řež	LR-0
Experimental Nuclear Reaction Data	EXFOR
Evaluated Nuclear Data File	ENDF
High Priority Request List	HPRL
High Purity Germanium	HPGe
International Atomic Energy Agency	IAEA
International Reactor Dosimetry and Fusion File	IRDFF
Japanese Evaluated Nuclear Data Library	JENDL
Joint Evaluated Fission and Fusion File	JEFF
Monte Carlo N-Particle Transport Code	MCNP
Net Peak Area	NPA
Prompt fission neutron spectra	PFNS
Research Center in Řež	CVŘ
Russian national library of neutron data	ROSFOND
Spectral average cross-section	SACS